

1 **Time-Of-Flight monitoring reveals higher sediment redistribution rates related to burrowing animals**
2 **than previously assumed**

3

4 *Paulina Grigusova*¹, *Annegret Larsen*², *Sebastian Achilles*¹, *Roland Brandl*³, *Camilo del Río*^{4,5}, *Nina Farwig*⁶,
5 *Diana Kraus*⁶, *Leandro Paulino*⁷, *Patricio Plissock*^{4,8,9}, *Kirstin Übernickel*¹⁰, *Jörg Bendix*¹

6

7

8 ¹ Laboratory for Climatology and Remote Sensing, Department of Geography, University of Marburg, 35037
9 Marburg, Germany; paulina.grigusova@staff.uni-marburg.de (P.G.); bendix@geo.uni-marburg.de (J.B.)

10 ² Soil Geography and Landscape, Department of Environmental Sciences,
11 Wageningen University & Research, 6700 AA Wageningen, The Netherlands; annegret.larsen@wur.nl

12 ³ Animal Ecology, Department of Biology, University of Marburg, 35032 Marburg, Germany;
13 brandlr@biologie.uni-marburg.de

14 ⁴ Facultad de Historia, Geografía y Ciencia Política, Instituto de Geografía, Pontificia Universidad Católica de
15 Chile, 782-0436 Santiago, Chile; plissock@uc.cl; cdelriol@uc.cl

16 ⁵ Centro UC Desierto de Atacama, Pontificia Universidad Católica de Chile, 782-0436 Santiago, Chile;
17 cdelriol@uc.cl

18 ⁶ Conservation Ecology, Department of Biology, University of Marburg, 35047 Marburg, Germany;
19 diana.kraus@biologie.uni-marburg.de (D.K.); nina.farwig@biologie.uni-marburg.de (N.F.)

20 ⁷ Facultad de Agronomía, Universidad de Concepción, 3780000 Chillán, Chile; lpaulino@udec.cl

21 ⁸ Facultad de Ciencias Biológicas, Departamento de Ecología, Pontificia Universidad Católica de Chile, 8331150
22 Santiago, Chile; plissock@uc.cl

23 ⁹ Center of Applied Ecology and Sustainability (CAPES), Pontificia Universidad Católica de Chile, 8331150
24 Santiago, Chile; plissock@uc.cl

25 ¹⁰ Earth System Dynamics, Department of Geosciences, University of Tübingen, 72076 Tübingen, Germany;
26 kirstin.uebernickel@uni-tuebingen.de

27

28 *Corresponding author:*

29 Paulina Grigusova

30 paulina.grigusova@staff.uni-marburg.de

31

32

33

34

35

36

37

38

39

40

41 **Abstract**

42 Burrowing animals influence surface microtopography and hillslope sediment redistribution, but changes often
43 remain undetected due to a lack of **automated** high resolution field monitoring techniques. In this study we
44 present a new approach to quantify microtopographic variations and surface changes caused by burrowing
45 animals and rainfall-driven erosional processes applied to remote field plots in arid and mediterranean Chile.
46 We compared the mass balance of redistributed sediment within plot areas affected and not affected by
47 burrowing animals, quantified the cumulative sediment redistribution caused by animals and rainfall, and
48 upscaled the results to a hillslope scale. The newly developed instrument, a Time-of-Flight camera, showed a
49 very good detection accuracy. **The animal-caused cumulative sediment redistribution was $14.62 \text{ cm}^3 \text{ cm}^{-2} \text{ year}^{-1}$**
50 **1 in the mediterranean and $9.57 \text{ cm}^3 \text{ cm}^{-2} \text{ year}^{-1}$ in the arid climate zone. The rainfall-caused cumulative**
51 **sediment redistribution within areas affected by burrowing animals was higher ($-10.44 \text{ cm}^3 \text{ cm}^{-2} \text{ year}^{-1}$) in the**
52 **mediterranean than the arid climate zone ($-1.41 \text{ cm}^3 \text{ cm}^{-2} \text{ year}^{-1}$). Daily sediment redistribution during rainfall**
53 **within areas affected by burrowing animals were up to 350% / 40% higher in the mediterranean / arid zone**
54 **compared to the unaffected areas, and much higher than previously reported in studies not based on continuous**
55 **microtopographic monitoring. Furthermore, 38% of the sediment eroding from the burrows accumulated within**
56 **the burrow entrance while 62% was incorporated into overall hillslope sediment flux. The animals burrowed**
57 **between on average 1.2 – 2.3 times a month and the burrowing intensity increased after rainfall. Our findings**
58 **can be implemented into long-term soil erosion models that rely on soil processes but do not yet include animal-**
59 **induced surface processes on microtopographical scales in their algorithms.**

60

61 **Keywords:** Biogeomorphology, bioturbation, sediment transport, burrowing animals, rainfall, Time-of-Flight
62 camera, Chile

63

64

65

66

67

68

69

70

71

72

73

74

75

76

77

78

79

80

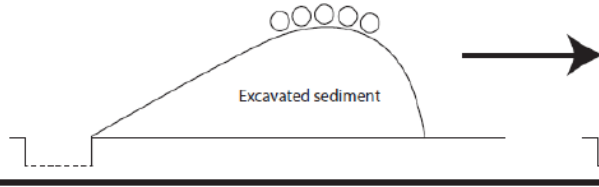
81

82 **Graphical abstract**

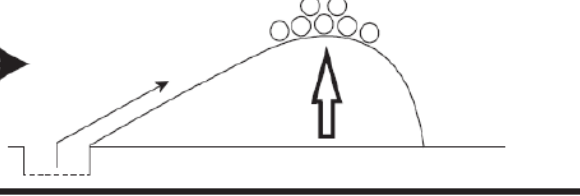
Animal-rainfall feedbacks

Arid (PdA)

(a) Initial surface

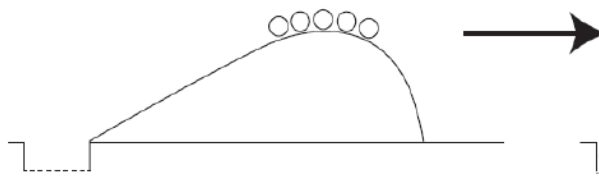


(b) Effect of animal burrowing

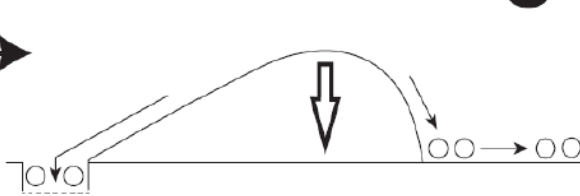


Mediterranean (LC)

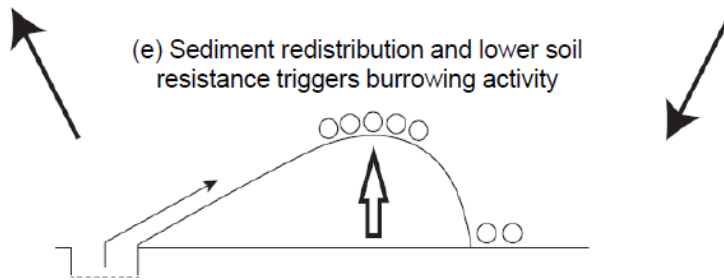
(c) Initial surface



(d) Rainfall driven sediment redistribution



(e) Sediment redistribution and lower soil resistance triggers burrowing activity



83

84

85 1. Introduction

86 Animal burrowing activity affects surface microtopography (Reichman und Seabloom 2002; Kinlaw
87 und Grasmueck 2012), surface roughness (Yair 1995; Jones et al. 2010; Hancock und Lowry 2021) and soil
88 physical properties (Ridd 1996; Yair 1995; Hall et al. 1999; Reichman und Seabloom 2002; Hancock und Lowry
89 2021; Coombes 2016; Larsen et al. 2021; Corenblit et al. 2021). Previous studies estimated both positive as
90 well as negative impacts of burrowing animals on sediment redistribution rates. The results were obtained by
91 applying tests under laboratory conditions using rainfall simulators, conducting several field campaigns weeks
92 to months apart, or by measuring the volume of excavated or eroded sediment in the field using methods such
93 as erosion pins, splash boards, or simple rulers (Imeson und Kwaad 1976; Reichman und Seabloom 2002;
94 Wei et al. 2007; Le Hir et al. 2007; Li et al. 2018; Li et al. 2019b; Li et al. 2019c; Voiculescu et al. 2019; Chen
95 et al. 2021; Übernickel et al. 2021b; Li et al. 2019a). Although burrowing animals are generally seen as
96 ecosystem engineers (Gabet et al. 2003; Wilkinson et al. 2009), their role in soil erosion, in general, and for
97 numerical soil erosion models, in particular, is, to date, limited to predictions of the burrow locations and particle
98 mixing at these locations (Black und Montgomery 1991; Meysman et al. 2003; Yoo et al. 2005; Schiffers et al.
99 2011). The complex interaction of sediment excavation and accumulation and erosion processes at the burrow
100 and hillslope scales are not yet included in the modelling, as for this, a suitable method capable of measuring
101 all occurred redistribution processes is needed.

102 The reason for this knowledge gap is that previous studies have not provided data on low magnitude
103 but frequently occurring sediment redistribution due to the specific limitations of their approaches. Field
104 experiments with, for example, rainfall simulators can unveil processes but cannot cover the time-dependant
105 natural dynamics of sediment redistribution. For data samplings that used methods such as erosion pins or
106 splash boards, the sites had to be revisited each time and the data were thus obtained only sporadically
107 (Imeson und Kwaad 1976; Hazelhoff et al. 1981; Richards und Humphreys 2010). Similarly, estimations of the
108 excavated sediment volume are currently limited to one-time measurements or studies conducted several
109 months apart (Black und Montgomery 1991; Hall et al. 1999; Yoo et al. 2005). We expect that non-continuously
110 conducted measurements do not include all frequently occurring excavation and erosion processes. For this,
111 a spatio-temporally high-resolution and continuous monitoring of sediment redistribution is needed.

112 High-resolution, ground-based imaging sensing techniques might overcome such aforementioned
113 problems. Terrestrial laser scanner systems have shown to be a suitable tool for estimation of sediment
114 redistribution and erosion processes (Nasermoaddeli und Pasche 2008; Afana et al. 2010; Eltner et al. 2016a;
115 Eltner et al. 2016b; Longoni et al. 2016). However, they are expensive and labour-intensive. A continuous,
116 automated monitoring of many mound areas in parallel is for this reason not possible. An already applied low-
117 cost (up to 5000\$) topographic monitoring technique is time-lapse photogrammetry which can be applied at
118 variable observation distances and scales (e.g. (James und Robson 2014; Galland et al. 2016; Eltner et al.
119 2017; Mallalieu et al. 2017; Kromer et al. 2019; Blanch et al. 2021). For this technique, the surface has to be
120 monitored under various angles for which several devices are needed to be installed in the field. In contrast,
121 Time-of-Flight (ToF) technology offers a new cost-effective possibility for a high-resolution monitoring of
122 sediment redistribution (Eitel et al. 2011; Hänsel et al. 2016) which can be achieved by a simple installation of
123 one device in the field.

124 In our study we developed, tested and applied a cost-effective Time-of-Flight camera for automated
125 monitoring of the rainfall and animal-driven sediment redistribution in areas affected by burrowing animals with
126 high temporal (four times a day) and spatial (6 mm) resolution. For this, we equipped several plots in remote

127 study sites in the Chilean arid and mediterranean climate zone. We selected these sites in order to analyse
128 sediment redistribution by burrowing activity of vertebrates under different rainfall regimes and as these sites
129 have been shown to be particularly strongly affected by burrowing activity (Grigusova et al. 2021). We
130 estimated the burrowing intensity and its dependence on rainfall. Then, we quantified the daily sediment
131 redistribution within areas affected and not affected by burrowing animals. We analysed the impacts of animal
132 burrowing activity and rainfall on the sediment redistribution and quantified the volume of sediment which is
133 additionally incorporated to the hillslope sediment flux due to the presence of burrows. Finally, we estimated
134 sediment redistribution on a burrow scale and upscaled sediment redistribution rates to the entire hillslopes.

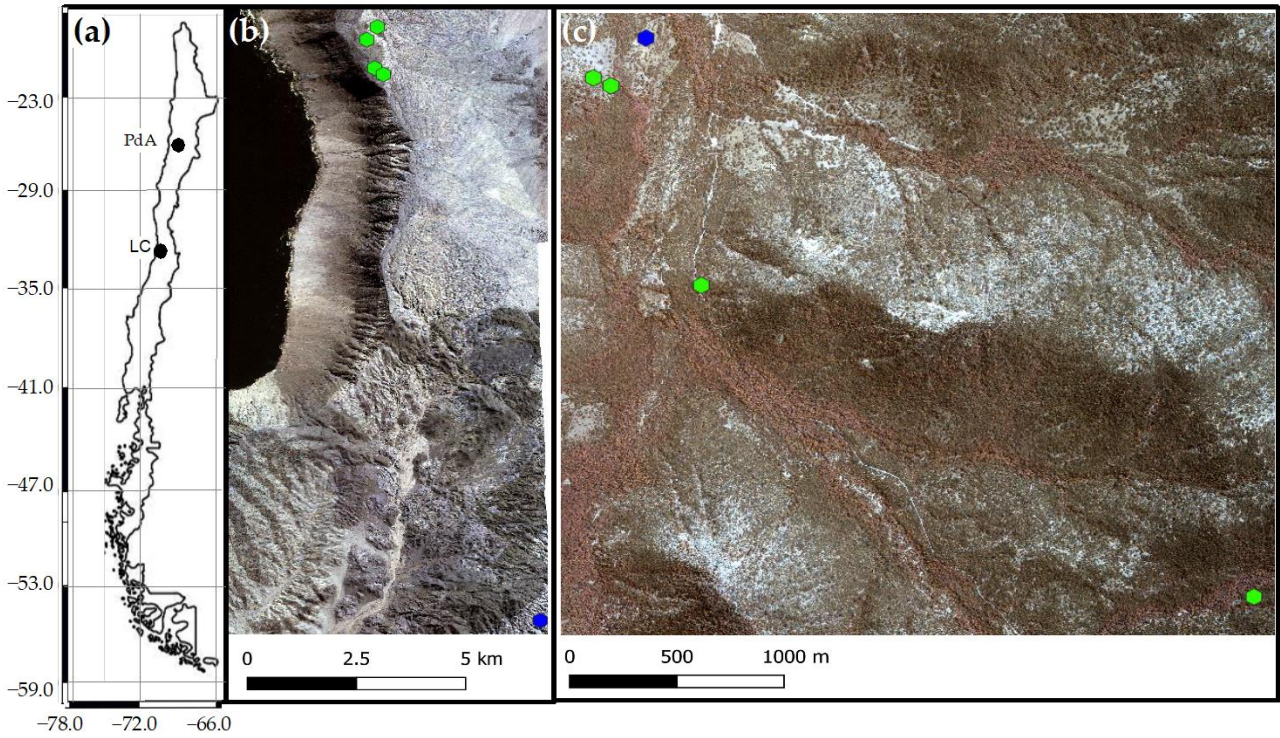
135

136 2. Study sites

137 Our study sites were located in the Chilean Coastal Cordillera in two climate zones (Fig. 1): in the National
138 Park Pan de Azúcar (further as Pan de Azúcar or PdA) and the National Park La Campana (further as La
139 Campana or LC). The Las Lomitas site in PdA is located in the arid climate zone of the Atacama Desert with a
140 precipitation rate of 12 mm year⁻¹, and it has a mean annual temperature of 16.8 °C (Übernicket et al. 2021a).
141 Here, the vegetation cover is below 5%, and it is dominated by small desert shrubs, several species of cacti
142 (*Eulychnia breviflora*, *Copiapoa atacamensis*) and biocrusts (Lehnert et al. 2018). LC is located in the
143 mediterranean climate zone with a precipitation rate of 367 mm year⁻¹ and a mean annual temperature of
144 14.1 °C (Übernicket et al. 2021a). LC is dominated by an evergreen sclerophyllous forest with endemic palm
145 trees, *Jubaea chilensis*. Both research sites have a granitic rock base, and the dominating soil texture is sandy
146 loam (Bernhard et al. 2018). In PdA, the study setup consisted of one north-facing and one south-facing
147 hillslope. The hillslope inclinations were ~20°, and a climate station was located ~15 km from the camera sites.
148 In LC, the setup consisted of two north-facing and one south-facing hillslopes. The hillslope inclinations were
149 ~25°, and a climate station was located ~250 m from the south-facing hillslope (Übernicket et al. 2021a).

150 Among the most common vertebrate burrowing animals are in PdA carnivores (*Lycalopex culpaeus*, *Lycalopex*
151 *griseus*); marsupials and rodents (*Phyllotis xanthopygus*, *Phyllotis limatus*, *Abrothrix andinus*) (Jimenez et al.
152 1992; Cerqueira 1985) and in LC rodents (*Octodon degus*, *Rattus norvegicus* and *Phyllotis darwini*) and
153 carnivores (*Lycalopex griseus*) (Muñoz-Pedreros et al. 2018)

154



155
 156 **Figure 1.** Location of the cameras and climate stations on which this study was based. Black points show the
 157 location of the research sites in Chile. The green points represent the camera plots, and the blue points the
 158 climate stations: (a) Location of study sites in Chile: PdA stands for Pan de Azúcar, LC for La Campana; (b)
 159 Study setup in Pan de Azúcar; (c) Study setup in LC. The background images in (b) and (c) are orthophotos
 160 created from WorldView-2 data from 19 July 2019. For exact latitude and longitude see Table A2.

161
 162 **3. Methodology**

163 **3.1 Time-of-Flight (ToF) principle**

164 A Time-of-Flight-based camera illuminates an object with a light source, usually in a non-visible
 165 spectrum, such as near-infrared, for a precise length of time. ToF cameras rely on the principle of measuring
 166 the phase shift, with different options to modulate the light source to be able to measure the phase shift. The
 167 here employed cameras used pulse-based modulation, meaning the light pulse was first emitted by the
 168 camera, then reflected from the surface, and finally measured by the camera using two temporary windows.
 169 The opening of the first window is synchronized with the pulse emission i.e. the receiver opens the window
 170 with the same Δt as the emitted pulse. Then, the second window is opened, for the same duration Δt , which is
 171 synchronised with the closing of the first window. The first temporary window thus measures the incoming
 172 reflected light while the light pulse is also still emitting from the camera. The second temporary window
 173 measures the incoming reflected light when no pulse is emitting from the camera. The captured photon number
 174 (i.e. measured by electrical charge) in both windows can be related according to equation 1 and the distance
 175 from the camera to the object can then be calculated as follows:

$$176 \quad d = \frac{1}{2} * c * t * \left(\frac{g_1}{g_1 + g_2} \right) \quad . \quad (1)$$

177 In Eq. (1), d (m) is the distance from the camera to the object, c (m s^{-1}) is the speed of light ($299,792,458 \text{ m s}^{-1}$),
 178 t (s) is the overall time of the illumination and measurement, g_1 is the ratio of the reflected photons to all
 179 photons accumulated in the first window, and g_2 the ratio of the reflected photons to all photons accumulated
 180 in the second window (Sarbolandi et al. 2018; Li 2014).

181 The sensor in our camera came from Texas Instruments and the data scan contained information on
182 320 x 240 points. The camera field of view (FOV) and the spatial resolution of the scans depended on the
183 height of the camera above the surface and camera orientation. The distance was calculated for every point,
184 and the object was saved in binary format as a collection of 3D points with x-, y- and z-coordinates. The point
185 clouds taken by the camera were transformed from the binary format to an ASCII format. Each point in the
186 point cloud was assigned to an x-, y- and z-coordinate. The coordinates were distributed within a three-
187 dimensional Euclidian space, with the point at the camera nadir (the centre of the camera sensor) being the
188 point of origin of the 3D Cartesian coordinate system. x- and y-coordinates describe the distance to the point
189 of origin (m). z-coordinate describes the distance (m) from the object to the camera. The lowest point of the
190 scanned surface thus has the highest z-coordinate value.

191

192 3.2 Data processing

193 The distortion caused by the hillslope and the camera angle was corrected for each point cloud as
194 follows:

$$195 z_{cor} = z_{uncor} - \tan(\alpha + \beta) * (y_1 - y_i) \quad . \quad (2)$$

196 In Eq. (2), z_{cor} is the corrected distance (m) between the camera and surface (m), z_{uncor} is the uncorrected z-
197 coordinate (m), α is the tilt angle of the camera ($^\circ$), β is the surface inclination ($^\circ$), and y_i (m) is the distance
198 between each point, and the point with i) an y-coordinate = 0 and ii) the same x-coordinate as the respective
199 point. The most frequent errors were identified and treated as follows. Due to the ambient light reaching the
200 camera sensor, the z-coordinate values of some of the points were incorrect (scattering error). To remove this
201 error, a threshold value was calculated for each point cloud:

$$202 \Omega = mean_{z_{cor}-coordinates} \pm sd_{z_{cor}-coordinates} \quad . \quad (3)$$

203 In Eq. (3), Ω is the threshold value, $mean_{z_{cor}-coordinate}$ is the average value, and $sd_{z_{cor}-coordinate}$ is the standard
204 deviation of the corrected z-coordinates (m). Then all points with a z-coordinate above and below this value
205 were deleted. Point clouds with more than 50% of points above the threshold value Ω were also not considered
206 for further processing. A drift error occurred when the z-coordinate values of around one-third of the point
207 clouds decreased by several centimetres from one point cloud to another. Here, the average z-coordinate of
208 ten point clouds before and after the drift were calculated, and the difference was added to z-coordinates of
209 the points affected by the drift. The corrected height values were then transformed into a digital surface model
210 (DSM).

211

212 3.3 Accuracy of the ToF cameras

213 The accuracy of the ToF camera was tested under laboratory conditions by recreating similar surface
214 conditions as in the field (sloping surface, covered by sediment). An artificial mound using sediment extracted
215 from a riverbank in central Germany was used, mimicking a mound created by a burrowing animal. During the
216 test, the camera was installed 100 cm above the surface. The camera FOV was 3 m² and the scan spatial
217 resolution was 6 mm. The surface was scanned twice by the ToF camera. Then 100 – 450 cm³ of sediment
218 was manually extracted from the mound. The volume of the extracted sediment was measured by a measuring
219 cup. After extraction, the surface was again scanned twice by the camera. The experiment was repeated 45
220 times with varying amounts of extracted sediment. The scans were transformed to point clouds in VoxelViewer-
221 0.9.10, and the point clouds were corrected according to Eq. (2) and (3). The z-coordinates of the two point
222 clouds before and two point clouds after the extraction were averaged. The standard deviation of the z-

223 coordinate of the two scans was 0.06 cm. Figure A1 shows the spatially distributed standard deviation. The
 224 deviation increases from the centre towards the corners of the scan. The mound was outlined and only the
 225 points representing the mound were used in the further analysis. The point clouds were then transformed into
 226 DSMs, and the differences between the time steps were calculated. A scan was taken of a smooth surface
 227 (linoleum floor) and a point cloud was created from the data. Then, we fitted a plane into the point cloud and
 228 calculated the distance between the plane and the camera sensor. The standard variation (0.17 cm) in the
 229 distance measurements was saved. Solely, the differences between the DSMs below this variation were
 230 considered in the calculation of the detected sediment extraction. The detected extracted sediment volume
 231 was then calculated for each experiment as follows:

$$232 \text{Vol}_{detected} = \sum_p^1 (DSM_{before} - DSM_{after}) * res^2 \quad , \quad (4)$$

233 In Eq. (4), $\text{Vol}_{detected}$ is the volume of the extracted sediment as detected by the camera (cm^3), p is the number
 234 of pixels, DSM_{before} (cm) is the DSM calculated from the scan taken before the extraction, DSM_{after} (cm) is the
 235 DSM calculated from the scan taken after the extraction, res (cm) is the resolution of the scan, which was 0.6
 236 cm. To evaluate the camera's accuracy, the measured volume of the extracted sediment was compared to the
 237 volume detected by the camera. The camera's accuracy was estimated between the detected volume and
 238 measured volume as follows:

$$239 MAE = \sum_1^n \frac{(\text{Vol}_{detected} - \text{Vol}_{measured})}{area} \quad . \quad (5)$$

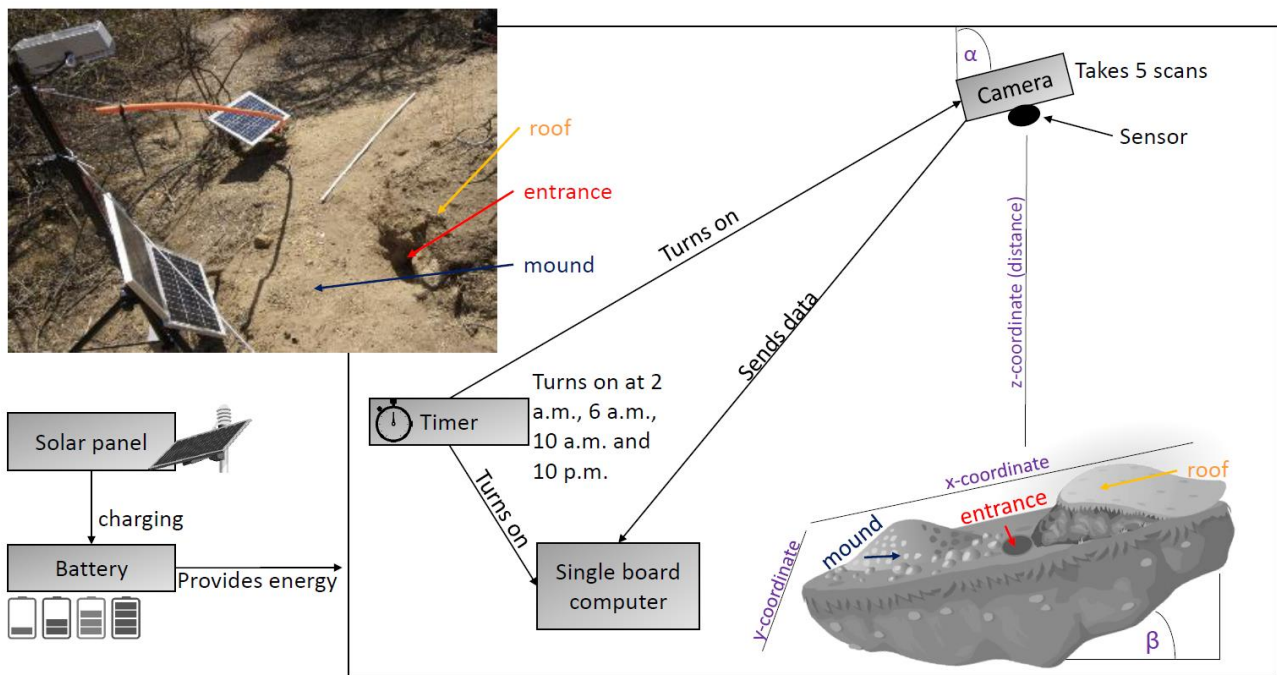
240 In Eq. (5), MAE (cm^3/cm^2) is the mean absolute error, n is the number of scans, $\text{Vol}_{measured}$ (cm^3) is the volume
 241 of the extracted sediment measured by the measuring cup, and the area is the total surface area monitored
 242 by the camera (cm^2).

243

244 3.4 Installation of the cameras in the field

245 We installed 8 custom-tailored ToF-based cameras on 4 hillslopes in two climate zones in areas
 246 including visible signs of bioturbation activity (burrows) and areas without visible signs of bioturbation (Fig. 2).
 247 The cameras were installed in LC on the north-facing upper hillslope (LC-NU), north-facing lower hillslope (LC-
 248 NL), south-facing upper hillslope (LC-SU) and the south-facing lower hillslope (LC-SL); in PdA on the north-
 249 facing upper hillslope (PdA-NU), north-facing lower hillslope (PdA-NL), south-facing upper hillslope (PdA-SU)
 250 and south-facing lower hillslope (PdA-SL). The custom-tailored cameras were installed during a field campaign
 251 in March 2019, the monitoring took place for seven months, and the data were collected in October 2019. The
 252 construction consisted of a 3D ToF-based sensor from Texas Instruments (Li, 2014), a RaspberryPi single board
 253 computer (SBC), a timer, a 12 V 12 Ah battery and three 20 W solar panels for unattended operation (Fig. 1).
 254 Solar panels were located at the camera pole and were recharging the battery via a charge controller. The
 255 camera was located approximately one meter above the surface, facing the surface with a tilt angle of 10
 256 degrees. The timer was set to close the electric circuit 4 times a day: at 1 a.m., 5 a.m., 8 a.m. and 10 p.m. At
 257 these times, the camera and the computer were turned on for 15 minutes. The camera turned on and took five
 258 scans delayed one second from each other and sent them to the SBC. Each camera had its own WiFi (Wireless
 259 Fidelity) and the data could be read from the SBC via Secure Shell (SSH). The cameras collected the data for
 260 the time period of 7 months.

261



262

263 **Figure 2.** Scheme and photo example of a Time-of-Flight-based camera installation in the field. The photo
 264 example is from upper north-facing hillslope in La Campana. Black boxes describe single installation parts.
 265 Purple descriptions are the variables needed for the correction of the scans. Roof, entrance and mound
 266 describe areas affected by the burrowing animal. The x-, y- and z-coordinates are 3D coordinates identifying
 267 the position of each point in space, where the x-coordinate is the length, y-coordinate is the width and the z-
 268 coordinate is the distance between the camera sensor and the surface. α is the inclination of the camera, and
 269 β is the surface inclination.

270

271 3.5 Delineation of the area affected and not-affected by burrowing animals

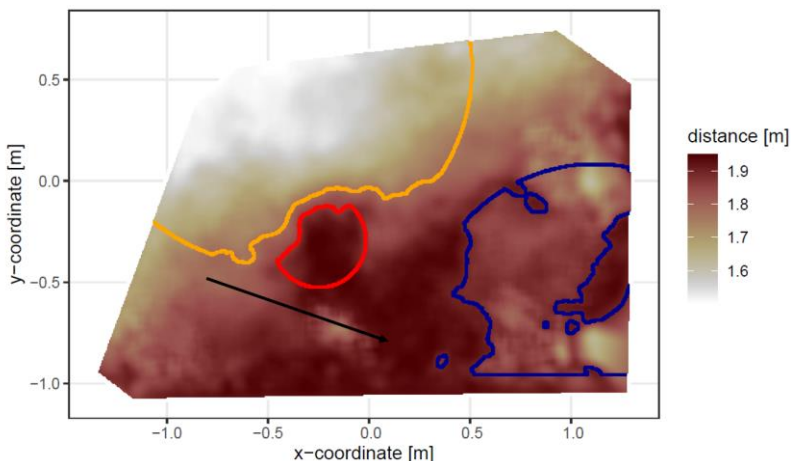
272 The surface area scanned by the cameras was divided by a delineation scheme into areas affected
 273 (A) and not (directly) affected (N) by burrowing animals. The affected areas included three sub-areas: (i) mound
 274 (M), (ii) entrance (E) and (iii) burrow roof (R). “Mound” describes the sediment excavated by the animal while
 275 digging the burrow. “Entrance” describes the entry to the animal burrow up to the depth possible to obtain via
 276 the camera. “Burrow roof” describes the part of the sediment above and uphill the burrow entrance (Bancroft
 277 et al. 2004). During the burrow’s creation, sediment was not only excavated but also pushed aside and uphill
 278 the entrance, which created the burrow’s roof. We assume that this elevated microtopographical feature then
 279 forms an obstacle for sediment transported from uphill, which leads to its accumulation in this area. The
 280 remaining surface within the camera’s FOV was classified as not affected (N) by the burrowing animal during
 281 the creation of its burrow.

282 For the delineation, we used the DSM calculated from the point cloud, and a slope layer calculated
 283 from the DSM (Horn 1981). The DSM had a size of 4 m² a resolution of 0.6 cm. Entrance was assigned to an
 284 area determined by a search algorithm starting at the lowest point of the DSM (pixel with the highest z-
 285 coordinate value). We increased the circular buffer around the starting point by one pixel until the average
 286 depth of the new buffer points was not higher than the height of the camera above the surface, or until the
 287 slope of at least 50% of the new buffer points was not 0. Then, we masked all pixels within the buffer with a
 288 depth lower than the average depth of the points within the buffer, which had a slope that was 0. The remaining

289 pixels belonged to the entrance area. Then, the surface scan was divided into an uphill and downhill part with
290 regards to the entrance position. Both the uphill and the downhill parts were subdivided into 16 squares, so
291 that each of the four quadrants within the 2D grid (x- and y-axis) contained four squares. The squares had size
292 of 0.5 m².

293 To delineate the mound in the downhill part, we first identified the highest points (pixel with the lowest z-
294 coordinate value) within all 16 squares. We then calculated the distance of these maxima to the entrance, and
295 the pixel located nearest to the entrance was identified as the highest point of the mound (i.e., seed point).
296 Consecutively, we increased the circular buffer around the seed point by one pixel until the average depth of
297 the new buffer points was not lower than the height of the camera above the surface, or until the slope of at
298 least 50% of the new buffer points was not 0. Then, we masked all pixels within the buffer with a depth higher
299 than the average depth of the points within the buffer, which had a slope that was 0. The remaining pixels were
300 classified as mound area. To delineate burrow roof, we used the same approach as for the delineation of
301 mound and applied it on the uphill part of the surface scan. We used the DEM and slope layers for the
302 delineation for several reasons. The distance from the surface to the camera was the most important parameter
303 to derive (i) the deepest point of the entrance and (ii) the highest point of the mound or burrow roof, as this
304 was (mostly) the closest point to the camera. After the angle correction of the z-coordinate according to chapter
305 3.2., the surface inclination of the areas without burrow was 0°, while the angle between the border of the
306 burrow entrance or mound and the not-affected surface was above 0°. Because neither the entrance nor the
307 mound have a perfect circular form, we would largely overestimate or underestimate the entrance or mound
308 size. Overestimate by not stopping the search algorithm until the angle between all new points of the buffer to
309 the rest of the buffer was 0°. Underestimate by stopping the algorithm when the angle of one point of the buffer
310 to the nearest point of the buffer was 0°. The value of 50% thus minimized the error. All pixels that were not
311 classified during the entire delineation process were treated as areas not affected by animals. Please note that
312 the areas termed “not affected” by the burrowing animals are areas adjacent to burrows. This does not imply
313 complete absence of animals, just no active burrowing.

314 The position and the boundaries of entrance, mound and burrow roof were validated visually (Fig. 3 and A2).



315
316 **Figure 3.** Corrected digital surface model of the camera on the upper north-facing hillslope in La Campana
317 with delineated areas. The point of origin of the coordinate system is at the camera nadir. Distance refers to
318 the distance between surface and camera. The red line delineates the burrow entrance, blue the mound and
319 orange the burrow roof. The area which was outside of any delineated area was classified as not affected by
320 animal burrowing activity. The arrow indicates a downhill direction of the hillslope.

321

322 In LC, the areas affected by the burrowing animal always consisted of an entrance, mound and burrow
323 roof. In PdA, there was no burrow roof on the upper hillslopes. Burrows without a burrow roof were located on
324 shallower parts of the hillslopes (up to an inclination of 5°), and the angle of the burrow entrance to the ground
325 was ~90°. Burrows with a burrow roof were located on steeper parts of the hillslopes (with an inclination above
326 5°), and the angle of the burrow entrance to the ground was ~45°.

327

328 **3.6 Calculation of animal-caused and rainfall-caused sediment redistribution**

329 The animal-caused sediment redistribution occurred when the animal actively reworked sediment
330 within its burrow. Under the assumption that the burrows are actively used by the animals, we defined four
331 cases when the sediment was redistributed due to the burrowing activity. For this, we pairwise compared the
332 DSMs of each scan with the scan saved before. The four cases were: (i) as the animal excavates sediment
333 from the entrance, the depth of the entrance must increase in the second scan; (ii) as the excavated sediment
334 accumulates on the mound, the height of the mound must increase in the second scan; (iii) as the burrowing
335 might lead to an expansion or a collapse of the burrow roof, an increase or decrease of the burrow roof must
336 occur between the scans; (iv) as the animal only digs within his burrow, no changes must occur between the
337 two scans within the area not affected by the animal. The animal-caused redistribution was then calculated for
338 these days as the volume of sediment redistributed within mound and burrow roof. The entrance was ignored
339 in the calculation. As the sediment excavated from the entrance accumulated on the mound and the sediment
340 accumulated within entrance collapsed from the burrow roof, by including the entrance in the calculation, these
341 sediment volumes would be counted twice.

342 The rainfall-caused sediment redistribution was calculated as follows: From the data from the climate stations
343 (Übernicker et al. 2021a), we calculated the daily precipitation in mm. The sediment redistribution recorded
344 immediately and within five scans before and after a rainfall event is defined to be the result of the rainfall
345 event. This was necessary as the climate stations are located up to a 15 km distance from the cameras (Fig.
346 1). If both animal-caused and rainfall-caused sediment redistribution took place, the following conditions
347 applied: i) rainfall event occurred, ii) burrow size changed as after digging (mound height increased, entrance
348 depth increased, burrow roof height increased or decreased), iii) sediment eroded from not affected areas.

349 We calculated the rainfall-caused sediment redistribution within (i) areas affected by the burrowing animal (i.e.,
350 entrance, mound and burrow roof) and (ii) within areas not affected by the burrowing animal. To estimate the
351 sediment volume which accumulated within the entrance, we also calculated the volume of redistributed
352 sediment solely (iii) within the entrance.

353

354 **3.7 Calculation of daily sediment mass balance budget**

355 The volume of the redistributed sediment was calculated daily and was then cumulated from the first
356 day of monitoring. For the calculation of the daily sediment redistribution, the change in the surface level
357 detected by the camera was calculated first. For each day, the scans from the day before and after the
358 respective day were averaged and subtracted. The average standard deviation of the z-coordinate of these
359 scans was 0.06 cm. As described in Section 2.2., all values with a difference below and above the threshold
360 value of 0.2 cm were set to 0. The redistributed sediment volume was then calculated from the surface change
361 for each pixel as follows:

$$362 \text{Vol}_{redistributed} = (S_b - S_a) * res^2 \quad . \quad (6)$$

363 In Eq. (6), $Vol_{redistributed}$ ($cm^3 pixel^{-1}$) is the volume of the calculated redistributed sediment, S_b (cm) the scan
 364 before, S_a (cm) the scan after the rainfall event and res is the spatial resolution (cm). Using the daily volume
 365 of the redistributed sediment per pixel, we calculated the daily mass balance budget by summing the volume
 366 of sediment eroding or accumulating within each delineated area.

367

368 **3.8 Calculation of the overall volume of redistributed sediment after the period of 7 months**

369 From the camera data, we calculated the average cumulative volume of redistributed sediment for the
 370 period of 7 months within affected ($Vol_{affected}$ ($cm^3 cm^{-2} year^{-1}$)) and non-affected ($Vol_{not\ affected}$ ($cm^3 cm^{-2} year^{-1}$))
 371 areas and the average sediment volume redistributed (excavated) by the animal (Vol_{exc} ($cm^3 cm^{-2} year^{-1}$)),
 372 separately for each site. We estimated the volume of sediment that was redistributed during rainfall events
 373 due to the presence of the burrow (Vol_{add} ($cm^3 cm^{-2} year^{-1}$)). Vol_{add} was calculated as the difference in the
 374 redistributed sediment volume between affected and non-affected areas according to Eq. (7).

$$375 Vol_{add} = (Vol_{affected} - Vol_{unaffected}) * 1.71, \quad (7)$$

376 Additionally, we calculated the average volume of the redistributed sediment per burrow ($Vol_{per\ burrow}$
 377 [$cm^3 burrow^{-1} year^{-1}$]):

$$378 Vol_{per\ burrow} = (Area_{burrow} * Vol) * 1.71 \quad (8)$$

379 In Eq. (8), $Area_{burrow}$ (cm^2) is the average size of the burrows that are monitored by the cameras; Vol is $Vol_{affected}$
 380 ($cm^3 cm^{-2} year^{-1}$), Vol_{exc} ($cm^3 cm^{-2} year^{-1}$) or Vol_{add} ($cm^3 cm^{-2} year^{-1}$).

381 We then upscaled the $Vol_{affected}$ ($cm^3 cm^{-2} year^{-1}$), Vol_{exc} ($cm^3 cm^{-2} year^{-1}$) and Vol_{add} ($cm^3 cm^{-2} year^{-1}$)
 382 to the hillslope using the same approach. Hillslope-wide upscaling of the results generated in this study was
 383 performed by using a previous estimation of vertebrate burrow density (Grigusova et al. 2021). In this study,
 384 the density of burrows was measured in situ within eighty 100 m^2 plots and then upscaled to the same hillslopes
 385 on which the cameras were located by applying machine-learning methods, using the UAV-data as predictors.
 386 Hence, the modelled burrows in the previous study were in fact areas affected by burrowing animals in this
 387 study. For upscaling, we applied a random forest model with recursive feature elimination. The model was
 388 validated by a repeated Leave-One-Out cross validation. The density of vertebrate burrows was between 6
 389 and 12 100 m^2 in LC and between 0 and 12 100 m^{-2} in Pan de Azúcar. Using the hillslope-wide predicted
 390 vertebrate burrow densities ($Dens_{burrow}$ (number of burrows 100 m^{-2})) from Grigusova et al. 2021, we estimated
 391 the volume of redistributed sediment for each pixel of the raster layers ($Vol_{per\ pixel}$ ($cm^3 m^{-2} year^{-1}$)) according
 392 to Eq. (9):

$$393 Vol_{per\ pixel} = Vol_{per\ burrow} * Dens_{burrow} * 1.17 \quad (9)$$

394 The average hillslope-wide volume of redistributed sediment ($Vol_{hillslope-wide}$ ($m^3 ha^{-1} year^{-1}$)) was then
 395 estimated as follows:

$$396 Vol_{hillslope-wide} = \sum_1^m Vol_{per\ pixel} * 0.001 * 1.71, \quad (10)$$

397 In Eq (10), m is the number of pixels. Please note that we used the volume of redistributed sediment monitored
 398 for 7 months to calculate the volume of sediment per year.

399

400 **4. Results**

401 **4.1 Camera accuracy and data availability**

402 The accuracy between the measured extracted sediment volume and sediment volume calculated
 403 from the camera scans was very high (MAE = 0.023 $cm^3 cm^{-2}$, $R^2 = 0.77$, SD = 0.02 $cm^3 cm^{-2}$, Fig. A3). The

404 accuracy between the calculated and measured extracted sediment was higher when the two scans taken
405 before as well as after the extraction of the sediment were averaged and the sediment volume was estimated
406 using these averaged scans. When calculating the redistributed sediment from solely one scan before and
407 after extraction, the accuracy slightly decreased ($MAE = 0.081 \text{ cm}^3 \text{ cm}^{-2}$, $R^2 = 0.64$). The cameras tended to
408 overestimate the volume of redistributed sediment. Six out of eight custom-tailored cameras collected data
409 over the seven-month period (Table A2). One camera collected data for a period of three months and one
410 camera stopped working a few days after installation. The quantity of usable point clouds taken at 1 a.m., 5
411 a.m. and 10 p.m. was higher than of point clouds taken at 8 a.m. Approximately 20% of points was removed
412 from the point clouds before final analysis due to the high scattering at the point cloud corners. After data
413 filtering (see Section 3.2.), 1326 scans were usable and for 86% of the days, at least one usable scan was
414 available. The usable scans were distributed continuously within the monitoring period.

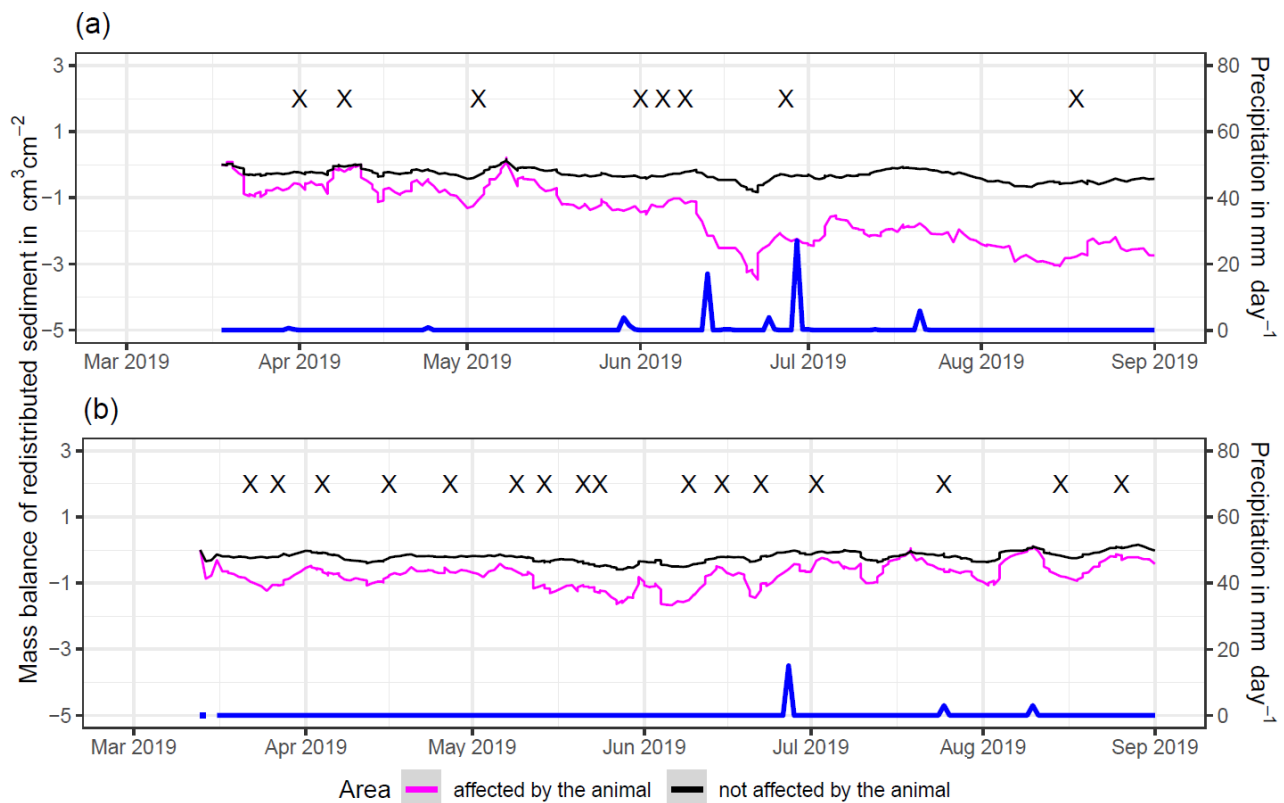
415

416 **4.3 Mass balance of redistributed sediment**

417 The cameras detected (i) sediment redistribution directly following rainfall events and (ii) due to the
418 burrowing activity in times without rainfall (Fig. 3, A4 and A5). In all cases, areas affected by burrowing activity
419 (entrance, burrow roof and mound) exhibited higher sediment redistribution rates than areas not affected by
420 burrowing. In addition, the volume of redistributed sediment by animal activity was higher after a rainfall event
421 occurred.

422 In the following, the dynamics are *exemplary* explained for four cameras. Animal burrowing activity
423 was detected seven times by the camera LC NU (Fig. 4a, A4, A5) during the monitoring period, by an increase
424 in sediment volume in the area delineated as mound. Simultaneously, the burrow entrance showed signs of
425 modification and sediment accumulation, but these changes were less clear. Overall, the volume of the
426 excavated soil varied. From April until June, up to $0.5 \text{ cm}^3 \text{ cm}^{-2}$ of sediment was excavated by the animal and
427 accumulated on the mound. From June until September, animal burrowing activity was detected at four time
428 slots (5 June 2019, 9 June 2019, 1 July 2019 and 18 August 2019) and sediment volume of up to $2 \text{ cm}^3 \text{ cm}^{-2}$
429 accumulated each time on the mound, burrow roof and within the entrance. During the rainfall events of up to
430 20 mm day^{-1} on 16 June 2019, 27 mm day^{-1} on 29 June 2019 and 7 mm day^{-1} on 13 July 2019, sediment
431 volume of up to $4 \text{ cm}^3 \text{ cm}^{-2}$ eroded, especially from the burrow roof and the mound while a sediment volume
432 of up to $1 \text{ cm}^3 \text{ cm}^{-2}$ accumulated within the entrance during each rainfall event. Camera LC-SL (Fig. A4, A5)
433 showed burrowing activities eight times and sediment volumes of up to $3 \text{ cm}^3 \text{ cm}^{-2}$ accumulated within the
434 entrance and burrow roof. The camera detected sediment erosion of up to $2 \text{ cm}^3 \text{ cm}^{-2}$ after a rainfall event of
435 27 mm day^{-1} on 27 July 2019. On the south-upper hillslope, the camera detected animal burrowing activity six
436 times, with a sediment accumulation of up to $3 \text{ cm}^3 \text{ cm}^{-2}$ (Fig. A2 and A3).

437 In contrast, camera PdA-NU pointed to animal burrowing activity up to 15 times where up to $1 \text{ cm}^3 \text{ cm}^{-2}$
438 of sediment volume was redistributed from the entrance to the mound (Fig. 4b, A4, A5). At the end of June
439 on 27 June 2019, a rainfall event of 1.5 mm day^{-1} occurred and up to $2 \text{ cm}^3 \text{ cm}^{-2}$ of sediment eroded from the
440 burrow roof and accumulated within the burrow entrance. We observed increased sediment redistribution by
441 the animal after the rainfall events. Camera PdA-SL evenly revealed animal burrowing activity up to 15 times
442 ((Fig. A4, A5)). The burrowing had a strong effect on the sediment redistribution. The rainfall event of 1.5 mm
443 day^{-1} on 27 June 2019 did not cause any detectable surface change.



444

445

446 **Figure 4.** Examples of the mass balance of redistributed sediment for areas affected and not affected by
 447 burrowing animals: (a) The record of the camera on the upper north-facing hillslope in la Campana showed
 448 that larger rainfall events cause a negative sediment balance (sediment loss), followed by a phase of positive
 449 sediment mass balance after approximately 3 days due to sediment excavation; (b) The record of the camera
 450 on the upper north-facing in Pan de Azúcar hillslope showed a similar pattern to the camera on the upper
 451 north-facing hillslope, but the phase of positive mass balance was delayed in comparison. The blue line is the
 452 daily precipitation in mm day⁻¹, and “X” marks the days at which animal burrowing activity was detected. Mass
 453 balances for all cameras are displayed in Fig. A2 and A3.

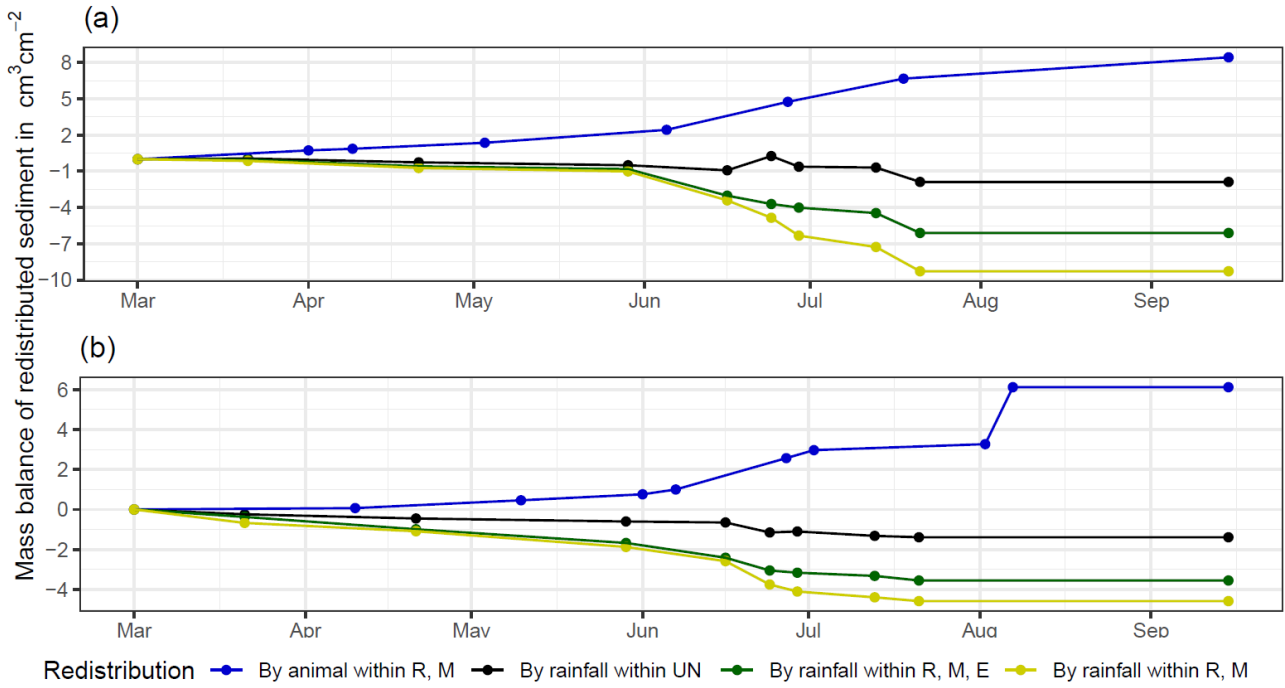
454

455 The analysis of cumulative volume of the redistributed sediment caused by burrowing animal activity
 456 and rainfall over the monitored period of seven months for all eight cameras showed a heterogeneous pattern.

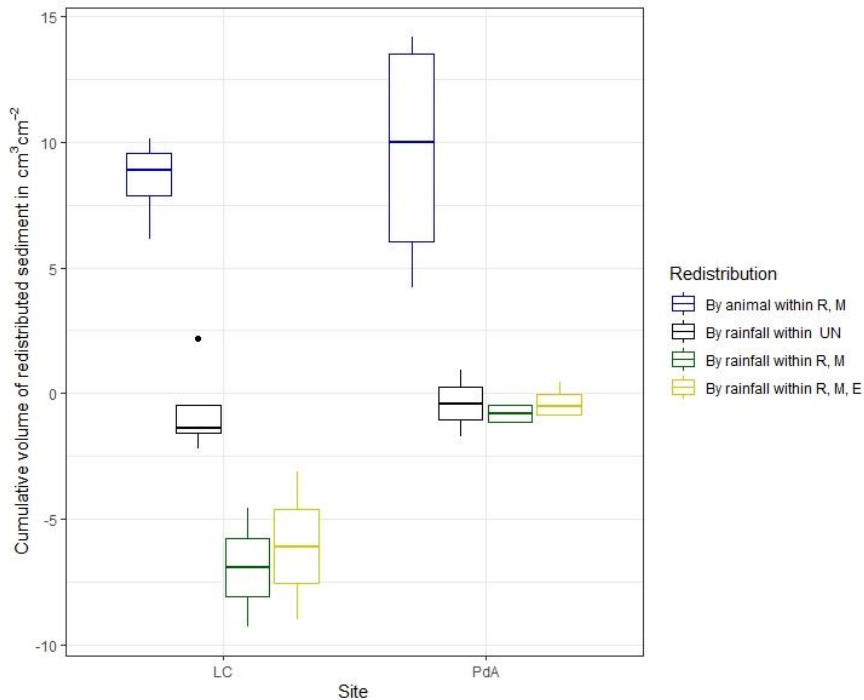
457 In LC, the cumulative volume of the sediment excavated by the animal within the burrow roof and
 458 mound increased continuously (Fig. 5, A7). Especially between the rainfall events from June until August, a
 459 cumulative volume of on average 6.5 cm³ cm⁻² was excavated by the animal. We calculated that, on average,
 460 8.53 cm³ cm⁻² cumulatively eroded from the burrow roof and mound; while 2.44 cm³ cm⁻² sediment volume
 461 accumulated within the entrance (Fig. 5, A7). These results indicate that 28% of sediment eroding from the
 462 burrow roof accumulated within the entrance, while over 62% of sediment eroded downhill. Averaged over all
 463 camera scans, 338% more sediment was redistributed by rain within the affected area compared to the non-
 464 affected area (Fig. 6).

465 In PdA, cameras continuously detected animal burrowing activity and excavation of the sediment (Fig.
 466 A7). The volume of the detected excavated sediment increased steadily within all cameras. The cumulative
 467 sediment accumulation surpasses the sediment eroded due to the rainfall. The volume of the sediment eroded

468 within the affected areas was 40% higher than within the non-affected areas. The results show that
 469 approximately 50% of the eroded sediment accumulated within the entrance (Fig. 6).
 470



471 Redistribution — By animal within R, M — By rainfall within UN — By rainfall within R, M, E — By rainfall within R, M
 472 **Figure 5.** Examples of the cumulative volume of redistributed sediment within affected and non-affected areas
 473 caused by animal burrowing activity or rainfall in mediterranean La Campana: (a) Upper north-facing hillslope;
 474 (b) Lower south-facing hillslope. Positive values indicate sediment accumulation. Negative values indicate
 475 sediment erosion. E is the burrow entrance; M is the mound; R is burrow roof; UN is the area not directly
 476 affected by the animal burrowing activity. Cumulative volumes for all cameras are in Fig. A7.



477 **Figure 6.** Cumulative volume of the redistributed sediment for all cameras. Positive values indicate sediment
 478 accumulation. Negative values indicate sediment erosion. Whiskers indicate the median of sediment
 479 redistribution. E is the burrow entrance; M the mound; R is the burrow roof; UN is area not affected by the
 480

481 animal burrowing activity; LC stands for National Park La Campana in the mediterranean climate zone; PdA
 482 stands for National Park PdA in the arid climate zone.

483

484 4.4 Volume of redistributed sediment

485 The average size of the burrows was 84.36 cm² (SD = 32.54 cm²) in LC and 91.35 cm² in PdA (SD = 8.53
 486 cm²). The animals burrowed on average 1.2 times month⁻¹ in LC and 2.33 times month⁻¹ in PdA. The volume
 487 of the excavated sediment was 102.22 cm³ month⁻¹ in LC and 124.89 cm³ month⁻¹ in PdA. Each time the
 488 animals burrowed, they excavated 42 cm³ sediment volume in LC and 14.33 cm³ sediment volume in PdA.
 489 The burrowing intensity increased in winter after the rainfall occurrences in LC and stayed constant during the
 490 whole monitoring period in PdA. The burrows deteriorate after rainfall events with a rate of 73.03 cm³ month⁻¹
 491 or 63.90 cm³ event⁻¹ in LC and 10.53 cm³ month or 24.57 cm³ event⁻¹.

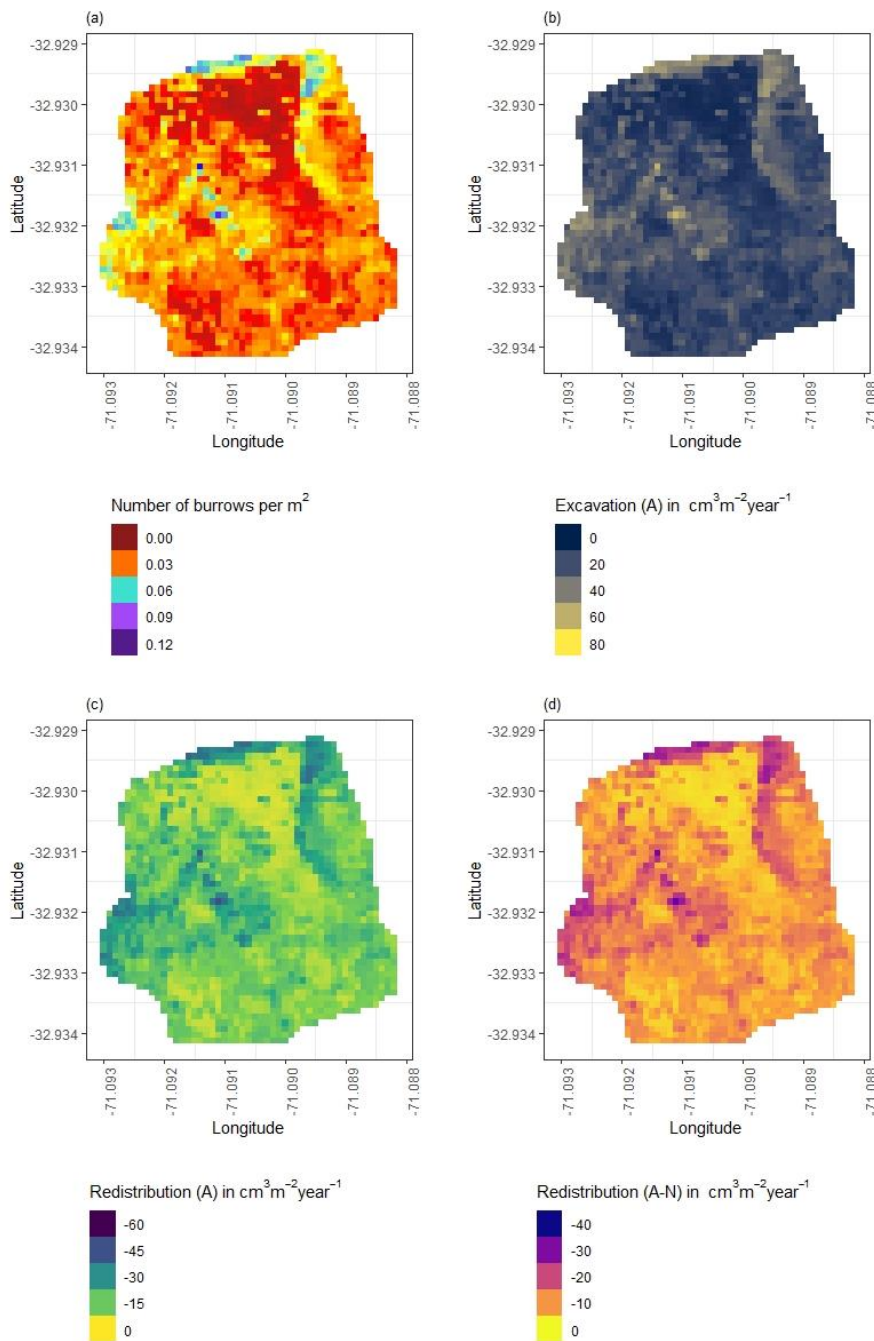
492 The overall volume of the sediment excavated by the animal and redistributed during rainfall events
 493 varied between the sites (Table 1). The volume of the sediment redistributed by the animal was lower in LC
 494 than in PdA. However, on the hillslope scale, a higher total area-wide volume of excavation was calculated for
 495 LC compared to PdA, due to the higher burrow density in LC. The volume of the sediment redistributed within
 496 the area affected by burrowing activity during rainfall events was higher in LC than in PdA. The volume of
 497 additionally redistributed sediment due to the presence of burrows was higher in LC than in PdA (Table 1, Fig.
 498 7).

499

500 **Table 1.** Summary of the volume of redistributed sediment, according to area and disturbance type. Vol_{exc}
 501 describes volume of the sediment excavated by the animals. Vol_{affected} describes volume of the sediment
 502 redistributed during rainfall events within affected areas. Vol_{add} describes the difference in redistributed
 503 sediment volume within affected and not affected area during rainfall.

Disturbance	Area	PdA	LC
Vol_{exc}	Affected area	16.41 cm ³ cm ⁻² year ⁻¹	14.62 cm ³ cm ⁻² year ⁻¹
	Per burrow	1498.66 cm ³ burrow ⁻¹ year ⁻¹	1226.61 cm ³ burrow ⁻¹ year ⁻¹
	Hillslope-wide	0.18 m ³ ha ⁻¹ year ⁻¹	0.67 m ³ ha ⁻¹ year ⁻¹
Vol_{affected}	Affected area	-1.97 cm ³ cm ⁻² year ⁻¹	-10.44 cm ³ cm ⁻² year ⁻¹
	Per burrow	-126.36 cm ³ burrow ⁻¹ year ⁻¹	-876.38 cm ³ burrow ⁻¹ year ⁻¹
	Hillslope-wide	-0.05 m ³ ha ⁻¹ year ⁻¹	-0.48 m ³ ha ⁻¹ year ⁻¹
Vol_{add}	Affected area	-1.18 cm ³ cm ⁻² year ⁻¹	-7.37 cm ³ cm ⁻² year ⁻¹
	Per burrow	-48.36 cm ³ burrow ⁻¹ year ⁻¹	-619.2 cm ³ burrow ⁻¹ year ⁻¹
	Hillslope-wide	-0.02 m ³ ha ⁻¹ year ⁻¹	-0.34 m ³ ha ⁻¹ year ⁻¹

504



505
 506 **Figure 7.** Example of the hillslope-wide volume of redistributed sediment for a time period of one year on the
 507 south-facing hillslope in La Campana: (a) Density of burrows as estimated by Grigusova et al. (2021); (b)
 508 Volume of the sediment excavated by the animals; (c) Volume of the sediment redistributed during rainfall
 509 events within affected areas; (d) Volume of additionally redistributed sediment during rainfall events due to the
 510 presence of the burrows. The values were calculated per burrow as stated in Section 3.7. by subtracting the
 511 sediment volume redistributed within animal-affected areas from the sediment volume redistributed within non-
 512 affected area and then upscaled. The letters in brackets indicate if the upscaling was conducted using data
 513 from affected or non-affected areas by burrowing animals. “A” stands for affected area. By “A-N”, the
 514 redistribution calculated from non-affected areas was subtracted from the redistribution calculated within
 515 affected areas to obtain the additional volume of redistributed sediment due to the burrows’ presence.
 516
 517

518 **5. Discussion**

519 Our results showed that the custom-made ToF device is a suitable tool for high-resolution, automated
520 monitoring of surface changes, applicable also in remote areas. The ability of a continuous observation of
521 sediment redistribution over a longer time during our study provided new insights into the importance of
522 burrowing animals for sediment redistribution. Our research reveals that the presence of vertebrate burrows
523 increases hillslope sediment redistribution rates much more than previously assumed (up to 208%). We
524 showed that the quantity of animal-related sediment redistribution, however, varied with rainfall occurrence,
525 with an increase in sediment redistribution between 40% in the arid research area and 338% percent in the
526 mediterranean research area.

527

528 **5.1 Suitability of the ToF method for surface monitoring**

529 The here proposed monitoring technique enables an automatic monitoring of surface changes on a
530 microtopographic scale, and its measurement continuity allows for the analysis of ongoing
531 biogeomorphological processes in high temporal resolution.

532 With regard to the costs, measurement frequency and sampling autonomy, the custom-made ToF
533 device stands in contrast to earlier studies that used laser scanning technology to monitor microtopographic
534 changes (Table A5). Previous studies mainly applied expensive laser scanning for the estimation of sediment
535 redistribution, and the research sites had to be personally revisited for each of the measurements
536 (Nasermoaddeli und Pasche 2008; Eltner et al. 2016a; Eltner et al. 2016b; Hänsel et al. 2016). The estimated
537 costs in studies using time-lapse photogrammetry were similar to our study (up to 5000\$) (James und Robson
538 2014; Galland et al. 2016; Mallalieu et al. 2017; Eltner et al. 2017; Kromer et al. 2019; Blanch et al. 2021).
539 However, for time-lapse monitoring, several devices needing different viewing angles increases installation
540 efforts significantly.

541 In terms of data quality, our ToF device is more precise or comparable to those employed in other
542 studies. The accuracy of the camera ($R^2 = 0.77$) was in the range of previous studies ($R^2 = 0.26$ – 0.83 (Eitel et
543 al. 2011), Table A5). The horizontal point spacing of our cameras was 0.32 cm, and the maximum number of
544 points per cm^2 was 8.5. These values are similar to previous studies in which the used devices had a horizontal
545 point spacing in the range of 0.25–0.57 cm (Kaiser et al. 2014; Nasermoaddeli und Pasche 2008)) (Table A5),
546 and the maximum number of points per cm^2 in a range of 1 point–25 points cm^{-2} (Eitel et al. 2011; Longoni et
547 al. 2016) (Table A5).

548 Our cameras tended to slightly overestimate or underestimate the volume of redistributed sediment.
549 This error occurs when the pulse reflects from several vertical objects such as walls or, in our case, branches
550 or stones and then enters the camera sensor. This phenomenon was also observed in previous studies
551 applying laser scanners and is inevitable if the goal is to study surface changes under natural field conditions
552 (Kukko und Hyypä 2009; Ashcroft et al. 2014). During operation of the cameras, we learnt that our newly
553 developed instruments are particularly capable of delivering usable scans at night. This is likely due to the
554 strong scattered sunlight reaching the camera sensor during the day, blurring the data (Li 2014). Thus, in future
555 studies, we recommend focusing on nocturnal operation to prevent light contamination from the surroundings.

556 We could thus prove that ToF cameras are a suitable and cost-effective method for a continuous
557 monitoring of sediment redistribution at a microtopographic scale without the need of time, labour and cost
558 intensive laser scanning/time-lapse photogrammetry campaigns.

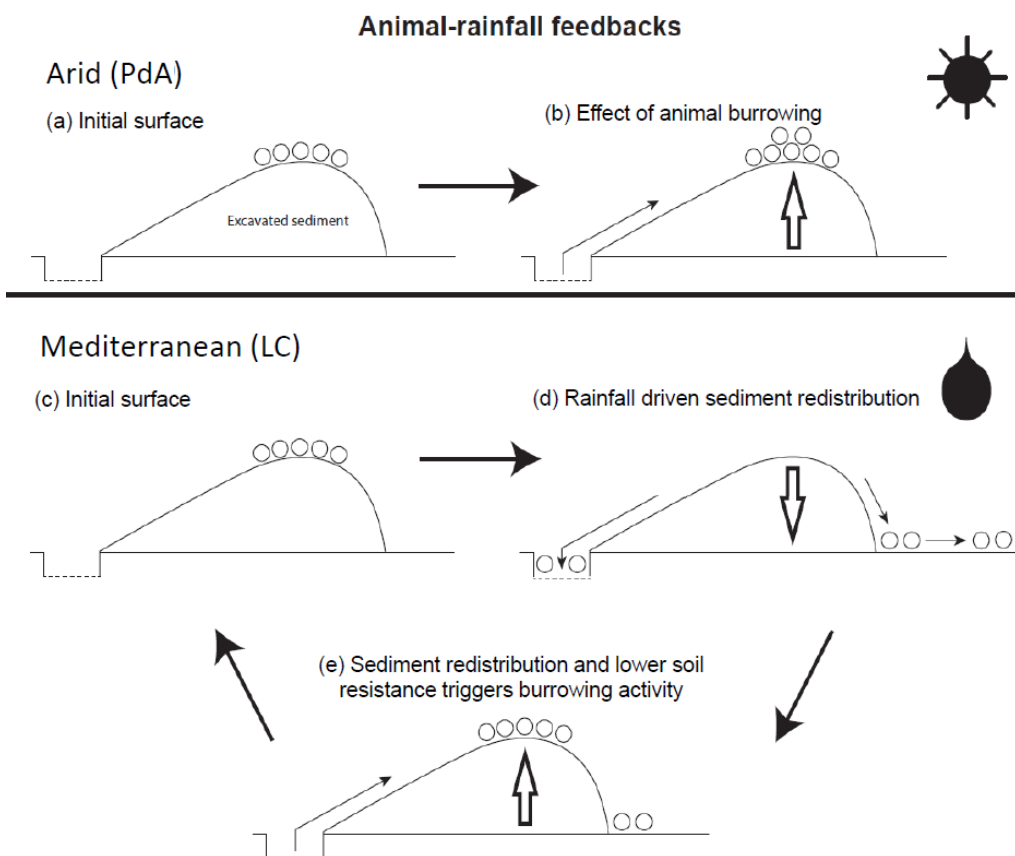
559

560 **5.2. Sediment Redistribution**

561 Our research reveals that the presence of vertebrate burrows generally increases hillslope sediment
562 redistribution. We show, however, that the ratio between the sediment redistribution caused by rainfall in the
563 areas affected and not affected by burrowing animals varies between climate zones. Sediment redistribution
564 in the affected areas was 40% higher at the arid research site, and at the mediterranean research site, it was
565 338% higher when compared to areas not affected by burrowing animals (Table A6).

566 By monitoring microtopographical changes in a high spatio-temporal resolution, we found that the
567 occurrence of larger rainfall events played a two-fold, accelerating role in influencing sediment redistribution
568 (Fig. 5, A4). Firstly, rainfall-runoff eroded burrow material caused increased sediment loss. This was followed
569 by animal burrowing activity after the rainfall. This means that rainfall triggered animal burrowing activity which
570 was very likely related to a lower burrowing resistance of the soil due to the increased soil moisture (Rutin
571 1996; Romañach et al. 2005; Herbst und Bennett 2006). This double feedback led to frequently occurring but
572 small redistribution rates. However, cumulatively, the mechanism increased downhill sediment fluxes. Previous
573 studies most likely missed this low magnitude but frequent surface processes due to a lower monitoring
574 duration and frequency, or artificial laboratory conditions, and thus, did not quantify the full volume of
575 redistributed sediment associated with burrowing activity. To quantify all occurred sediment redistribution
576 processes, a continuous surface monitoring, like the here presented, is needed.

577



578

579 **Figure 8.** Scheme of animal-driven and rainfall-driven sediment redistribution processes in both investigated
580 climate zones: (a) Describes the initial surface of the burrow before the start of a sediment redistribution
581 process, and (b) the animal excavation process in the arid climate zone. Here, due to rarely occurring rainfall
582 events, sediment redistribution is mostly controlled by the animal burrowing activity; (c) describes the initial

583 burrow surface in the mediterranean climate zone, (d) the process of sediment redistribution during a rainfall
584 event and (e) the subsequent animal burrowing activity. Burrowing is triggered by decreased soil resistance
585 due to the increased soil moisture after rainfall as well as by sediment accumulation within the burrow's
586 entrance. Burrowing activity leads to a new supply of sediment being excavated to the surface. In the
587 mediterranean climate zone, sediment redistribution is controlled by both animal burrowing activity and rainfall.
588 The alternating excavation and erosion process ultimately lead to an increase in redistribution rates.

589
590 Our results indicate an up to 338% increase in the sediment volume redistributed during rainfall events
591 measured in the areas affected by burrowing animals when compared to not affected areas. In contrast to our
592 result, the maximum increase estimated in previous studies was 208% (Table A6, (Imeson und Kwaad 1976).

593 The two climate zones also show different patterns: In the mediterranean climate, the contribution of
594 animals' (vertebrates') burrowing activity appear larger than previously observed by using field methods such
595 as erosion pins or splash traps (from -3% until - 208%, Table A6, (Imeson und Kwaad 1976; Hazelhoff et al.
596 1981; Black und Montgomery 1991). In contrast, in arid PdA, our study found a much smaller increase (40%,
597 Table A6) in the sediment volume redistributed during rainfall events measured in the areas affected by
598 burrowing animals when compared to not affected areas. This is lower than previously estimated (125%, Table
599 A6, (Black und Montgomery 1991) However, solely one rainfall event above 0.2 mm day⁻¹ occurred during our
600 monitoring period. Hence, we conclude that the contribution of burrowing activity of animals to hillslope
601 sediment transport is much larger in areas with frequent rainfall events than previously thought, while it has
602 been realistically estimated by previous studies for areas with rare rainfall events (Table A6).

603 Overall, our study revealed a strong impact of animal excavation processes on sediment redistribution
604 in the mediterranean climate zone (0.67 m³ ha⁻¹ year⁻¹), which were more in a range of excavated volume
605 observed in previous studies by bears and porcupines (0.49 m³ ha⁻¹ year⁻¹, Table A8, (Hall et al. 1999) than
606 rodents (0.02 m³ ha⁻¹ year⁻¹, (Hall et al. 1999). The estimated sediment excavation in the arid climate zone
607 (0.18 m³ ha⁻¹ year⁻¹, Fig. A4, Table A8) was in the order of magnitude of previous studies (0.05–0.2 m³ ha⁻¹
608 year⁻¹, Table A8, (Black und Montgomery 1991; Yoo et al. 2005). Our results thus suggest that animal
609 burrowing activity is an important part of the environmental mechanisms leading to increased sediment fluxes
610 in wetter (as a consequence of animal-triggered excavation and rainfall-triggered erosion) and drier (as a
611 consequence of animal-triggered excavation) regions (Fig. 5).

612 Magnitudes of sediment volume redistributed within areas affected by burrowing animals similar to our
613 results were previously obtained solely in studies applying rainfall simulators. These studies estimated an
614 increase in the volume of sediment redistributed during rainfall events, measured in the areas affected by
615 burrowing animals when compared to not affected areas, to be between 205% and 473% (Table A6, (Li et al.
616 2018; Chen et al. 2021). However, a rainfall simulator can only provide data on surface processes within a plot
617 of a few m² in size and under ideal laboratory conditions while ignoring the uphill microtopography, vegetation
618 cover and distribution (Iserloh et al. 2013), which were shown to reduce erosion rates. More importantly, the
619 rainfall intensity on hillslopes decreases with (i) the angle of incidence of the rain, (ii) the inclination of the
620 surface and iii) the relative orientation of the sloping surface to the rain vector (Sharon 1980). When simulating
621 a rainfall event with the same rainfall volume as in the field, the rain is induced directly over the treated surface
622 and has thus a higher velocity which leads to an increased splash erosion than under natural conditions (Iserloh
623 et al. 2013). We thus propose that the rainfall experiments overestimate the erosion rate while the correct
624 erosion rate can be measured solely under field conditions.

625 Cumulative sediment redistribution within burrow roof, mound and entrance was, on average, 28%
 626 lower than cumulative sediment redistribution only within the mound and the burrow roof (Figure A7). These
 627 results suggest that 28% of the eroded sediment from animal mounds and burrow roofs is re-accumulated
 628 within the burrow entrance during rainfall-runoff events, and the remaining 62% is incorporated into overall
 629 hillslope sediment flux. Our numbers contrast with previous studies, which quantified that about 58% of the
 630 sediment excavated by animals will accumulate back in the burrow entrance and only 42% is incorporated to
 631 downhill sediment flux (Andersen 1987; Reichman und Seabloom 2002). Hence, our results indicate not only
 632 higher redistribution rates within areas affected by burrowing animals but also point to much higher supply of
 633 sediment to the downhill sediment flux than previously thought.

634 Our cost-effective ToF device provides data on surface changes in a high spatio-temporal resolution.
 635 The high temporal resolution was able to unravel ongoing low magnitude but frequent animal excavation and
 636 erosion processes. The high spatial resolution enabled us to estimate the exact volume of sediment fluxes
 637 from the burrows downhill. The here presented results indicate that the contribution of burrowing animals on
 638 the burrow as well as on the hillslope scale was much higher than previously assumed. Our results can be
 639 integrated into long-term soil erosion models that rely on soil processes and improve their accuracy by
 640 including animal-induced surface processes on microtopographical scales in their algorithms.

641
 642

643 **Funding:** This study was funded by the German Research Foundation, DFG [grant numbers
 644 BE1780/52-1, LA3521/1-1, FA 925/12-1, BR 1293-18-1], and is part of the DFG Priority Programme
 645 SPP 1803: EarthShape: Earth Surface Shaping by Biota, sub-project “Effects of bioturbation on rates
 646 of vertical and horizontal sediment and nutrient fluxes”.

647 **Institutional Review Board Statement:** Not applicable.

648 **Informed Consent Statement:** Not applicable.

649 **Acknowledgments:** We thank CONAF for the kind support provided during our field campaign.

650 **Competing interests:** There is no conflict of interest.

651 **Author contribution:** JB, AL and SA planned the campaign; PG and SA performed the measurements; PG
 652 analysed the data and wrote the manuscript draft; AL, JB, NF, RB, KÜ, LP, CR, DK and PP reviewed and edited
 653 the manuscript.

654 **Code/Data availability:** Code and all raw data can be provided by the corresponding author upon request.

655

656 **Appendices**

657 **Table A1.** List of abbreviations

α [°]	Tilt angle of the camera
b [°]	Surface inclination
Ω	Threshold value for the scan scattering error
A	Affected area
Affected area	Area directly affected by the burrowing animal
Area_{burrow}	mean in the field measured size of the burrows which are monitored
Area	total surface area monitored by the camera
BD	Bulk density

c [m/s]	Speed of light
D	Distance from the camera to the object
Dens_{burrow}	Burrow density
DSM	Digital surface model
DSM_{after}	DSM calculated from the scan taken after the extraction
DSM_{before}	DSM calculated from the scan taken before the extraction
Entrance	entrance to the animal burrow
g [-]	ratio [-] of the reflected photons to all photons
LC	National Park LC
LC-NL	Camera in LC on the lower north-facing hillslope
LC-NU	Camera in LC on the upper north-facing hillslope
LC-SL	Camera in LC on the lower south-facing hillslope
LC-SU	Camera in LC on the upper south-facing hillslope
MAE	Mean absolute error
MAP [°]	Mean annual precipitation
m.a.s.l.	Meters above sea level
MAT	Mean annual temperature
mClay [%]	Mean content of clay
mean_{z-coordinate}	Mean value of the z-coordinates
Mound	the sediment excavated by the animal while digging the burrow
mSand [%]	Mean content of sand
mSilt [%]	Mean content of silt
N	Number of scans
N	Not affected area
Not affected area	Area not directly affected by the burrowing animal
PdA	National Park Pan de Azúcar
PdA-NL	Camera in PdA on the lower north-facing hillslope
PdA-NU	Camera in PdA on the upper north-facing hillslope
PdA-SL	Camera in PdA on the lower south-facing hillslope
PdA-SU	Camera in PdA on the upper south-facing hillslope
Res	Resolution
Roof	sediment pushed aside and uphill the entrance during burrow creation
S_a	scan after the rainfall event
S_b	scan before the rainfall event
SBC	Single board computer
sd_{z-coordinate}	standard deviation of the z-coordinates
SSH	Secure shell
t [s]	Overall time of camera illumination
TOC [%]	Total organic carbon
ToF	Time-of-Flight

Vol_{affected}	volume of redistributed sediment within affected area
Vol_{detected}	volume of the extracted sediment as detected by the camera
Vol_{add}	difference in redistributed sediment volume between affected and not affected areas
Vol_{exc}	Volume of the sediment excavated by the animal
Vol_{hillslope-wide}	Hillslope-wide volume of redistributed sediment
Vol_{measured}	volume of the extracted sediment measured by the measuring cup
Vol_{per burrow}	Volume of redistributed sediment per burrow
Vol_{per pixel}	Volume of redistributed sediment per pixel
Vol_{redistributed}	volume of the calculated redistributed sediment
Vol_{not affected}	volume of redistributed sediment within not affected area
y_i	distance of the point to the point of origin at the camera nadir
z_{cor}	Corrected z-coordinate
z_{uncor}	Uncorrected z-coordinate

658

659 **Table A2.** Number of usable scans for each camera

Camera	Latitude	Longitude	Number of scans	Percentage of usable scans taken at 1am / 5am / 8am / 10pm	Time period
PdA-NU	-25.98131	-70.6166	238	29 / 27 / 20 / 24	18.3.-18.9.
PdA-NL	-25.98277	-70.61278	52	24 / 0 / 40 / 36	27.3.-31.5
PdA-SU	-25.97477	-70.61641	351	30 / 26 / 32 / 11	16.3.-19.9.
PdA-SL	-25.97177	-70.61409	167	48 / 38 / 7 / 8	16.3.-19.9.
LC-NU	-32.95230	-71.06231	215	37 / 20 / 8 / 33	9.3.-9.9.
LC-NL	-32.93928	-71.08613	3	-	6.3.-12.9
LC-SU	-32.93078	-71.09066	160	22 / 28 / 26 / 25	28.3.-22.5
LC-SL	-32.93110	-71.08987	167	27 / 25 / 22 / 26	16.3.-19.9.

660

661 **Table A3.** Summary of the volume of redistributed sediment, according to area and disturbance type. Vol_{exc}
662 describes volume of the sediment excavated by the animals. Vol_{affected} describes volume of the sediment
663 redistributed during rainfall events within affected areas. Vol_{add} describes the difference in redistributed
664 sediment volume within affected and not affected area during rainfall.

Disturbance	Area	PdA	LC
Vol_{exc}	Affected area	16.41 cm ³ cm ⁻² year ⁻¹	14.62 cm ³ cm ⁻² year ⁻¹
	Per burrow	1498.66 cm ³ burrow ⁻¹ year ⁻¹	1226.61 cm ³ burrow ⁻¹ year ⁻¹
	Hillslope-wide	0.18 m ³ ha ⁻¹ year ⁻¹	0.67 m ³ ha ⁻¹ year ⁻¹
Vol_{affected}	Affected area	-1.97 cm ³ cm ⁻² year ⁻¹	-10.44 cm ³ cm ⁻² year ⁻¹
	Per burrow	-126.36 cm ³ burrow ⁻¹ year ⁻¹	-876.38 cm ³ burrow ⁻¹ year ⁻¹
	Hillslope-wide	-0.05 m ³ ha ⁻¹ year ⁻¹	-0.48 m ³ ha ⁻¹ year ⁻¹

Vol_{add}	Affected area	-1.18 cm ³ cm ⁻² year ⁻¹	-7.37 cm ³ cm ⁻² year ⁻¹
	Per burrow	-48.36 cm ³ burrow ⁻¹ year ⁻¹	-619.2 cm ³ burrow ⁻¹ year ⁻¹
	Hillslope-wide	-0.02 m ³ ha ⁻¹ year ⁻¹	-0.34 m ³ ha ⁻¹ year ⁻¹

665

666

667 **Table A4.** Summary of the volume of redistributed sediment for the period of 7 months, according to area and
668 disturbance type. Vol_{exc} describes volume of the sediment excavated by the animals. Vol_{affected} describes
669 volume of the sediment redistributed during rainfall events within affected areas. Vol_{add} describes the difference
670 in redistributed sediment volume within affected and not affected area during rainfall.

Disturbance	Area	PdA	LC
Vol_{exc}	Affected area	9.57 cm ³ cm ⁻² 7 months ⁻¹	8.53 cm ³ cm ⁻² 7 months ⁻¹
	Per burrow	874.22 cm ³ burrow ⁻¹ 7 months ⁻¹	715.52 cm ³ burrow ⁻¹ 7 months ⁻¹
	Hillslope-wide	0.11 m ³ ha ⁻¹ 7 months ⁻¹	0.39 m ³ ha ⁻¹ 7 months ⁻¹
Vol_{affected}	Affected area	-1.15 cm ³ cm ⁻² 7 months ⁻¹	-6.09 cm ³ cm ⁻² 7 months ⁻¹
	Per burrow	-73.71 cm ³ burrow ⁻¹ 7 months ⁻¹	-511.22 cm ³ burrow ⁻¹ 7 months ⁻¹
	Hillslope-wide	-0.03 m ³ ha ⁻¹ 7 months ⁻¹	-0.28 m ³ ha ⁻¹ 7 months ⁻¹
Vol_{add}	Affected area	-0.69 cm ³ cm ⁻² 7 months ⁻¹	-4.30 cm ³ cm ⁻² 7 months ⁻¹
	Per burrow	-28.21 cm ³ burrow ⁻¹ 7 months ⁻¹	-361.20 cm ³ burrow ⁻¹ 7 months ⁻¹
	Hillslope-wide	-0.01 m ³ ha ⁻¹ 7 months ⁻¹	-0.2 m ³ ha ⁻¹ 7 months ⁻¹

671

672 **Table A5.** Review of studies which used laser scanners for the estimation of surface processes.

Reference	R²	Error	Horizontal point spacing	Points per cm²	Model	Price
Our results	0.77	0.15 cm	0.32 cm	8.5	Texas Instruments OPT3101	900 \$
(Eitel et al. 2011)	0.23-0.86	0.07 cm	NA	25	Leica ScanStation 2	102 375 \$
(Eltner et al. 2013)	NA	0.4 cm	NA	6.4	Riegl LMS-Z420i	16 795
(Kaiser et al. 2014)	NA	NA	0.57 cm	NA	Riegl LMS-Z420i	16 795
(Longoni et al. 2016)	NA	NA	NA	1	Riegl LMS-Z420i	16 795
(Morris et al. 2011)	NA	0.5 cm	NA	NA	Maptek I-Site 4400LR	240 000

673
674
675

(Nasermoaddeli und Pasche 2008)	NA	0.2 cm	0.25 cm	NA	Leica HDS 2500	Cyrax	4500 \$	
(Thomsen et al. 2015)	NA	NA	0.4 cm	NA	Leica ScanStation 2		102 375 \$	

Table A6. Review of studies which estimated the sediment redistribution in areas affected and not affected areas and the proposed impact.

Reference	Climate	Animals	Method	Monitoring period	Frequency	Affected areas	Not affected areas	Impact
Our results	arid	vertebrates	scanning	7 months	Daily	1.97 cm ³ cm ⁻² year ⁻¹	1.39 cm ³ cm ⁻² year ⁻¹	+40 %
Our results	Mediterranean	vertebrates	scanning	7 months	daily	10.44 cm ³ cm ⁻² year ⁻¹	1.39 cm ³ cm ⁻² year ⁻¹	+338 %
(Imeson und Kwaad 1976)	continental	rodents	erosion pins	15 months	monthly	20 mm		NA
(Imeson und Kwaad 1976)	continental	rodents	splash boards	15 months	monthly	91.75g 24.49 cm ⁻² = 3.75 cm ³ cm ⁻²	94g	-3%
(Imeson und Kwaad 1976)	continental	rodents	rainfall simulation (7.5 cm / hour intensity)	One-time measurement	NA	0.2 g – 0.73 g	0.009 g – 0.23 g	+208 %
(Imeson 1977)	continental	vertebrates	rainfall simulation	One-time measurement	NA	0.18-0.3 100 J ⁻¹ m ⁻² rain	0.146 100 J ⁻¹ m ⁻² rain	+123 %
(Hazelhoff et al. 1981)	continental	earthworms	splash traps	12 months	monthly	NA	NA	+180 %
(Black und Montgomery 1991)	arid	pocket gopher	erosion pins	10 months	2 months	NA	NA	+125 %
(Hakonson 1999)	temperate	pocket gophers	rainfall simulation	2 years	2 – 3 weeks	2.4 – 8.7 mg ha ⁻¹	4.4 – 15 mg ha ⁻¹	-43%

			r (60 mm / hour)							
(Li et al. 2018)	temperate	mole crickets	rainfall simulation (36 mm / hour)	One time measurement	15	22.1 g 115 cm ⁻² = 5.2 cm ³ cm ⁻²	5 g 123 cm ³ = 1.09 cm ³ cm ⁻²	+473 %		
(Li et al. 2018)	temperate	mole crickets	rainfall simulation (36 mm / hour)	One time measurement	15	35.3 g 220.5 cm ⁻² = 6.24 cm ³ cm ⁻²	5 g 123 cm ³ = 1.09 cm ³ cm ⁻²	+473 %		
(Chen et al. 2021)	lab	chinese zocor	rainfall simulation (80 mm / hour)	One-time measurement	3	2,69 g cm ⁻² = 2.69 cm ³ cm ⁻²	0,88 g cm ³ = 0.88 cm ³ cm ⁻²	+205 %		

676

677

678 **Table A7.** Review of studies which estimated the sediment redistribution in areas affected by burrowing
679 animals, average burrow density as found in the literature and area-wide yearly contribution of burrowing
680 animals to sediment redistribution.

Climate	Animals	Affected areas	Average burrow density	Average burrow size	Area-wide redistribution
Arid	vertebrates	1.97 cm ³ cm ⁻² year ⁻¹	0-12 10 m ⁻² = 0-1.2 m ⁻² (Grigusova et al. 2021)	91.35 cm ²	1.18 cm ³ ha ⁻² year ⁻¹
mediterranean	vertebrates	10.44 cm ³ cm ⁻² year ⁻¹	6-12 10 m ⁻² = 0.6 – 1.2 m ⁻² (Grigusova et al. 2021)	84.36 cm ²	0.67 m ³ ha ⁻¹ year ⁻¹
Continental	rodents	91.75g cm ⁻² = 3.75 cm ³ cm ⁻² (Imeson und Kwaad 1976)	24.49 14 625 m ⁻² = 0.02 m ⁻² (Pang und Guo 2017)	24.49 cm ² (Imeson und Kwaad 1976)	0.183 m ³ ha ⁻¹ year ⁻¹
Temperate	mole crickets	22.1 g 115 cm ⁻² = 5.2 cm ³ cm ⁻² (Li et al. 2018)	405 ha ⁻¹ (Castner und Fowler 1984)	115 cm ² (Li et al. 2018)	0.24 m ³ ha ⁻¹ year ⁻¹

Temperate	mole crickets	35.3 g cm ⁻² = 6.24 cm ³ cm ⁻² (Li et al. 2018)	220.5 405 (Castner und al. 2018)	ha ⁻¹	220.5 cm ² (Li et al. 2018)	0.56 m ³ ha ⁻¹ year ⁻¹
Lab	chinese zocor	2,69 g cm ⁻² = 2.69 cm ³ cm ⁻² (Chen et al. 2021)	94.69 2500m ⁻² = 0.04 m ⁻² = 400 ha ⁻¹		1256 cm ²	1.35 m ³ ha ⁻¹ year ⁻¹

681

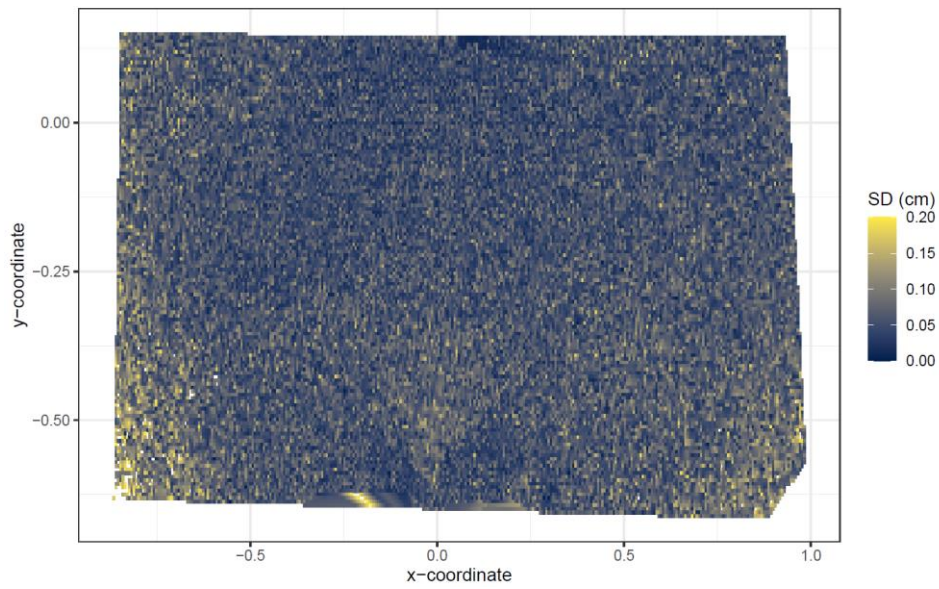
682

Table A8. Review of studies which estimated the volume of sediment excavated by burrowing animals.

	Climate	Animals	Method	Monitoring period	Frequency	volume of the excavated sediment
Our results	arid	vertebrates	Scanning	7 months	daily	0.18 m ³ ha ⁻¹ year ⁻¹
Our results	mediterranean	vertebrates	Scanning	7 months	daily	0.67 m ³ ha ⁻¹ year ⁻¹
(Black und Montgomery 1991)	arid	porcupines	mound volume	3 years	yearly	0.2 m ³ ha ⁻¹ year ⁻¹
(Black und Montgomery 1991)	arid	isopods	mound volume	3 years	yearly	0.11 m ³ ha ⁻¹ year ⁻¹
(Black und Montgomery 1991)	arid	pocket gopher	mound volume	2 years	3 model runs	0.05 – 0.11 m ³ ha ⁻¹ year ⁻¹
(Rutin 1996)	subtropical	scorpions	mound volume	6 months	2-29 days	0.42 m ³ ha ⁻¹ year ⁻¹
(Hall et al. 1999)	alpine	rodents	mound volume	1 year	yearly	0.02 m ³ ha ⁻¹ year ⁻¹
(Hall et al. 1999)	alpine	bears	mound volume	1 year	yearly	0.49 m ³ ha ⁻¹ year ⁻¹
(Yoo et al. 2005)	arid	pocket gopher	mound volume	1 year	One model run	0.1-0.2 m ³ ha ⁻¹ year ⁻¹

683

684

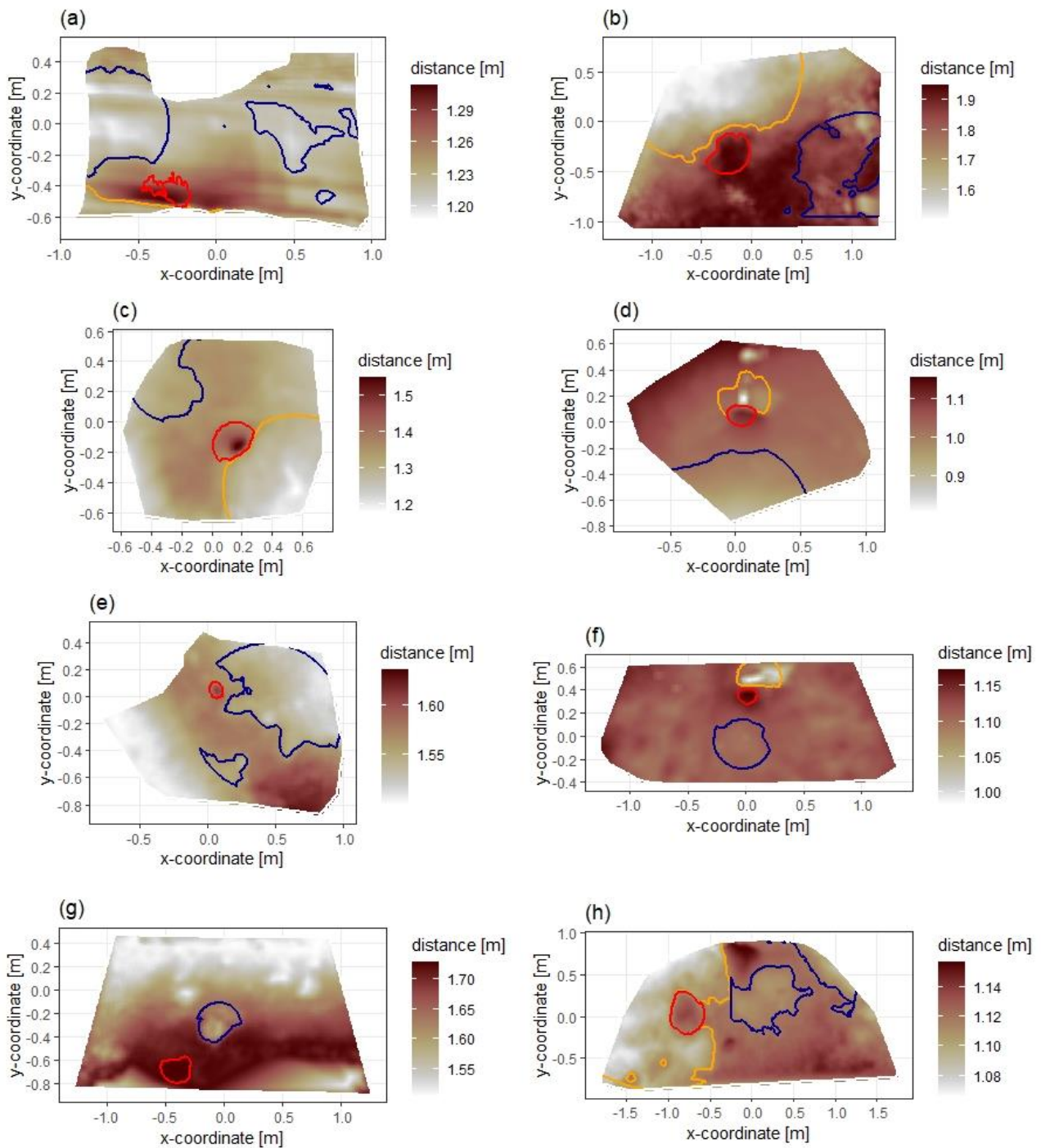


685

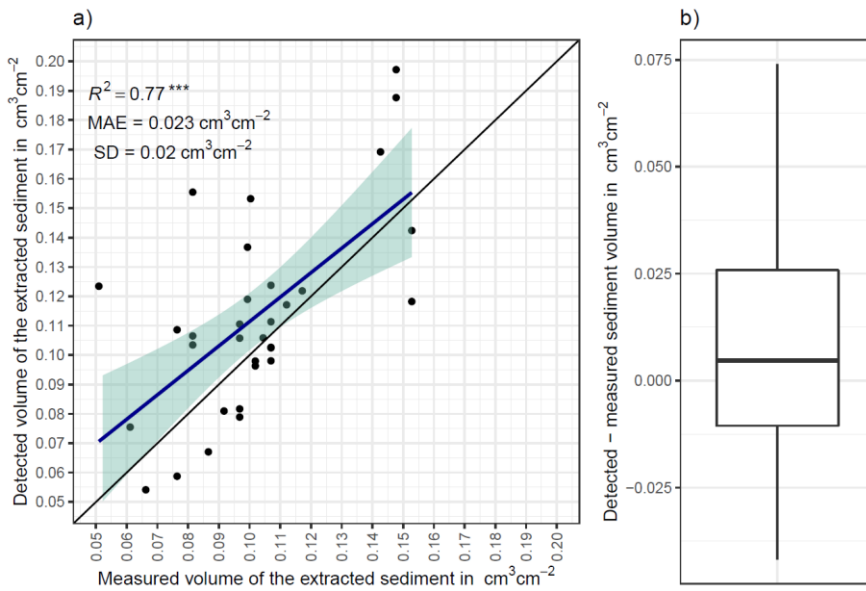
686 **Figure A1.** Standard deviation of the z-coordinate of unprocessed five scans showed exemplary for the camera
687 on the upper north-facing hillside. SD is standard deviation. The error increases with distance from the camera
688 nadir point. The standard deviation was here calculated from scans before any corrections.

689

690



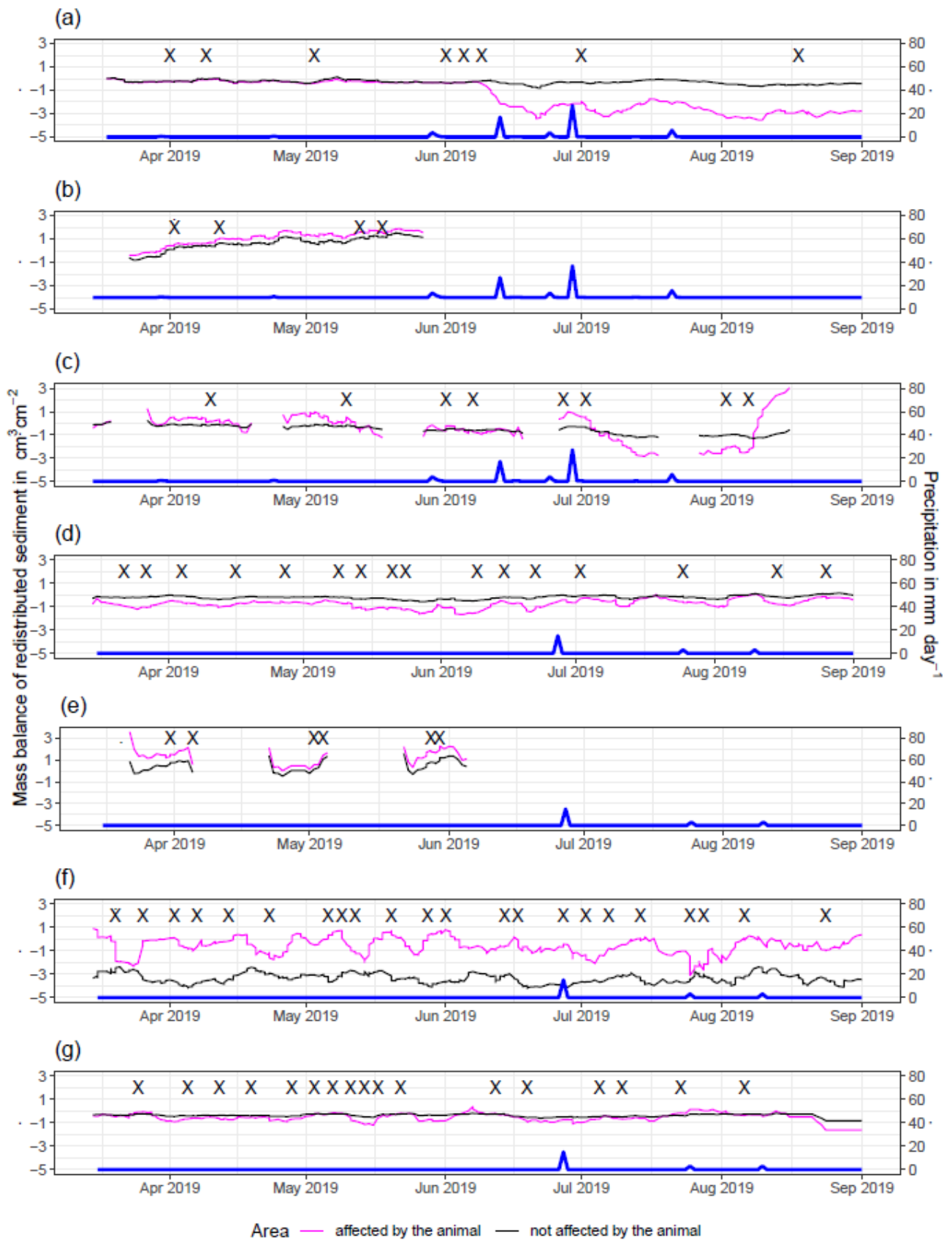
691
 692 **Figure A2.** Delineation of the areas. The point of origin of the coordinate system is at the camera nadir. Depth
 693 is the distance between the surface and the camera. Red is the outline of the burrow entrance. Green is the
 694 outline of mound. Orange is the outline of burrow roof. Area which is not outlined is area not directly affected
 695 by the animal burrowing activity. Arrow indicates downhill direction of the hillslope. (a) LC-NU. (b) LC-NL (c)
 696 LC-SU. (d) LC-SL. (e) PdA-NU. (f) PdA-NL. (g) PdA-SU. (h) PdA-SL.

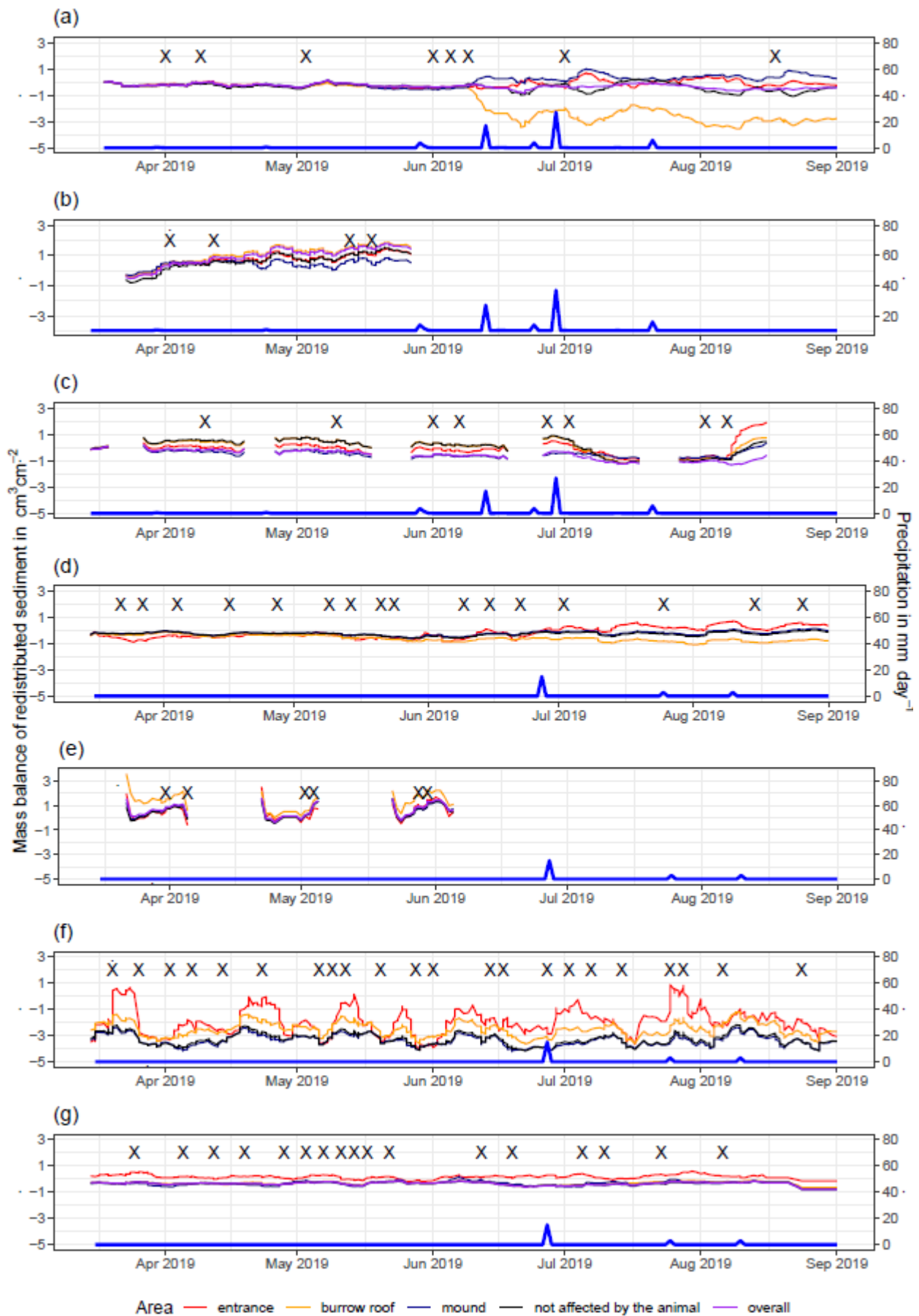


697

698 **Figure A3.** a) Estimation of Time-of-Flight camera accuracy based on averaging two surface scans before and
 699 after the sediment extraction under controlled conditions. The x-axis shows the exact sediment volume
 700 measured with a cup. The y-axis represents the volume of the sediment calculated from the camera scans
 701 (according to Equation (4)). The blue line is the linear regression calculated from the measured and detected
 702 volume. The green shadow shows the confidence interval of 95% for the linear regression slope. $^{***}p \leq 0.001$.
 703 MAE is the mean absolute error, SD is standard deviation and R^2 the coefficient of determination. b) Measured
 704 sediment volume subtracted from the detected sediment volume for all measurements.

705

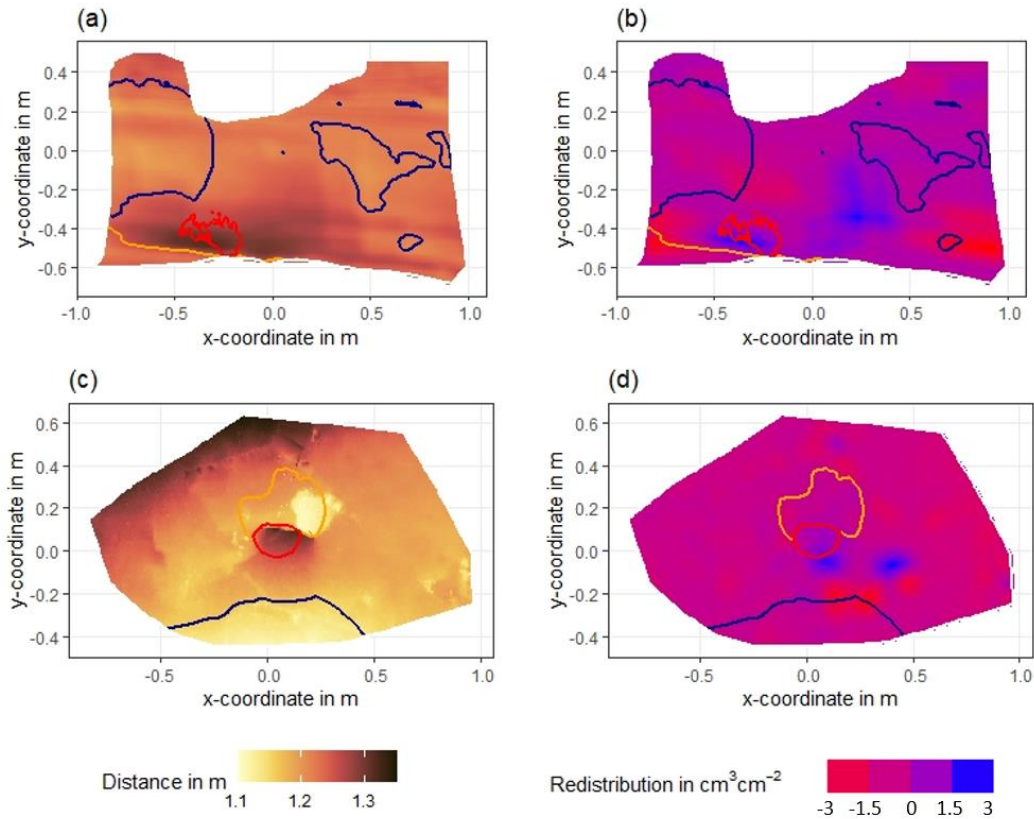




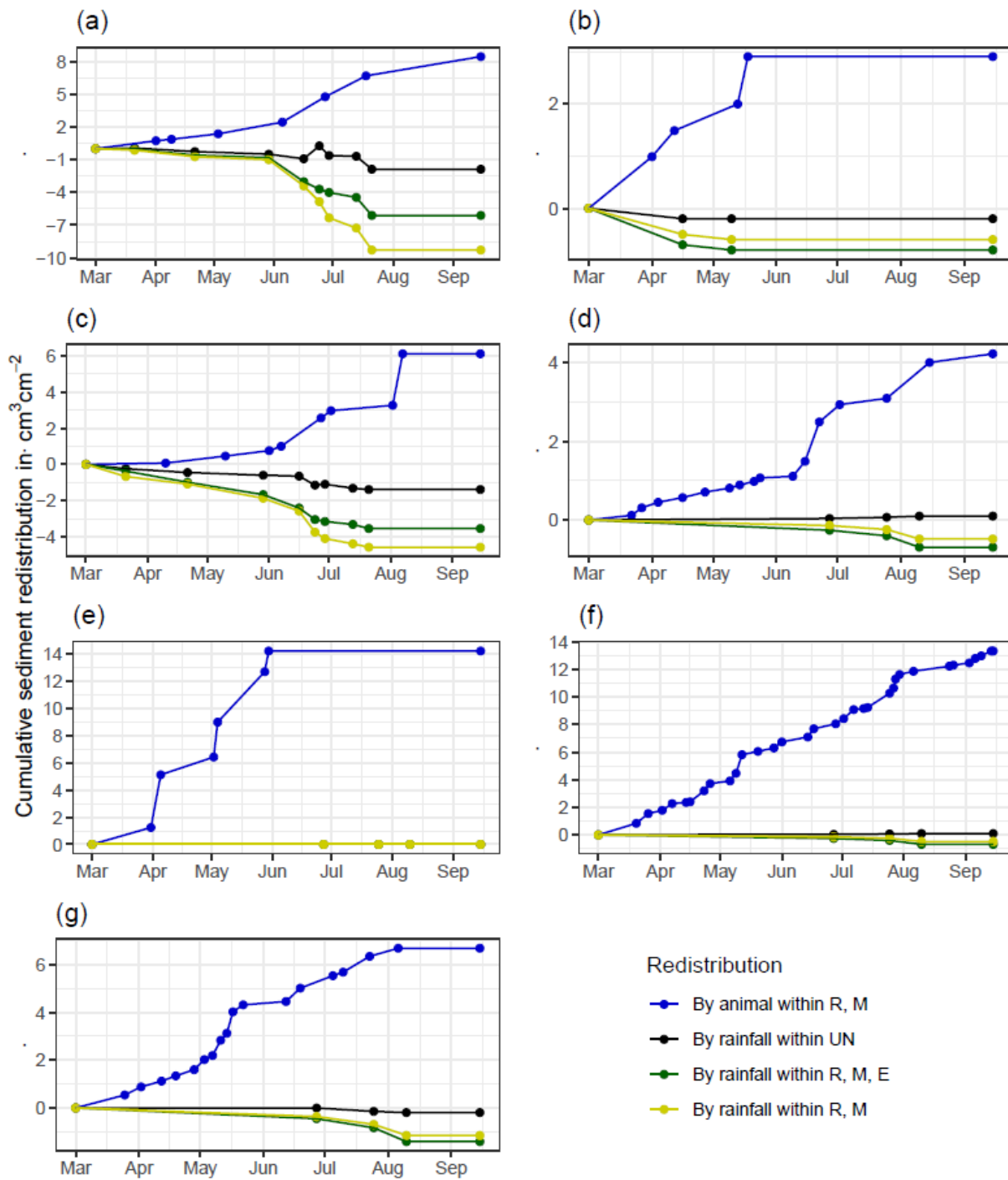
710

711 **Figure A5.** Sediment mass balance for the period of 7 months separately for all delineated areas as measured

712 by the cameras. (a) LC-NU. (b) LC-SU. (c) LC-SL. (d) PdA-NU. (e) PdA-NL. (f) PdA-SU. (g) PdA-SL. For
 713 abbreviations see Table A1.
 714



715
 716 **Figure A6.** Examples of surface scans showing the digital surface model (DSM) before a rainfall event (a, c)
 717 at two camera locations in La Campana, and the calculated volume of redistributed sediment (b, d) after the
 718 rainfall event: (a) DSM of a scan from the camera on the upper north-facing hillslope in La Campana; (b)
 719 Detected sediment redistribution ($\text{cm}^3 \text{cm}^{-2}$) on the upper north-facing hillslope in La Campana after a rainfall
 720 event of 17.2 mm day^{-1} ; (c) DSM of a scan from the camera on the upper south-facing hillslope in La Campana;
 721 (d) Detected sediment redistribution ($\text{cm}^3 \text{cm}^{-2}$) on the upper south-facing hillslope after a rainfall event of 17.2
 722 mm day^{-1} . Red is the outline of the burrow entrance. Green is the outline of mound. Orange is the outline of
 723 the burrow roof. The area which is not outlined is the area not directly affected by animal burrowing activity.
 724 Redistribution is the volume of the redistributed sediment, either accumulated (positive value) or eroded
 725 (negative value) per $\text{cm}^3 \text{cm}^{-2}$. After the rainfall events, sediment mostly accumulated within the burrow
 726 entrance or near mounds and eroded from burrow roofs and mounds.
 727
 728



729

730

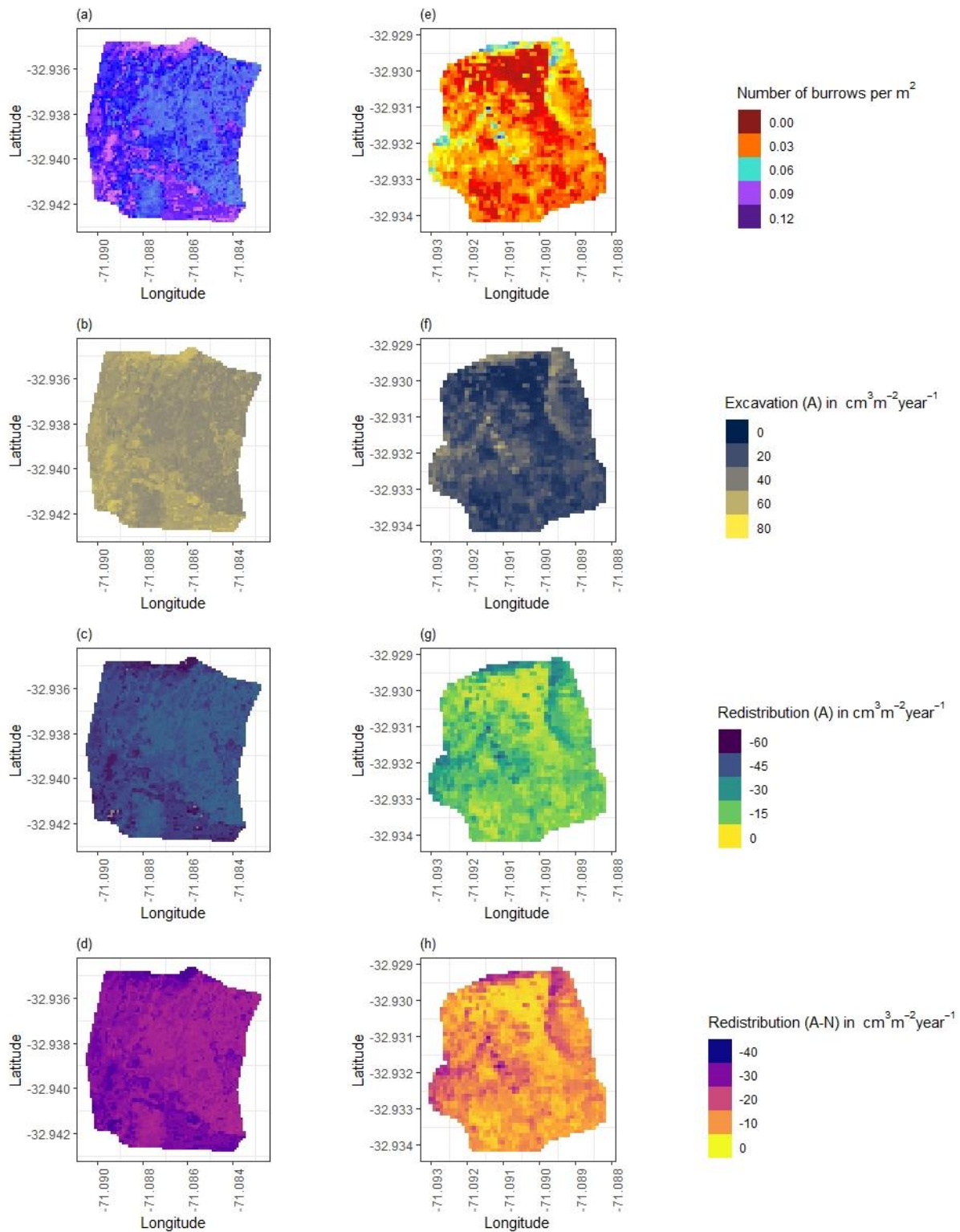
731

732

733

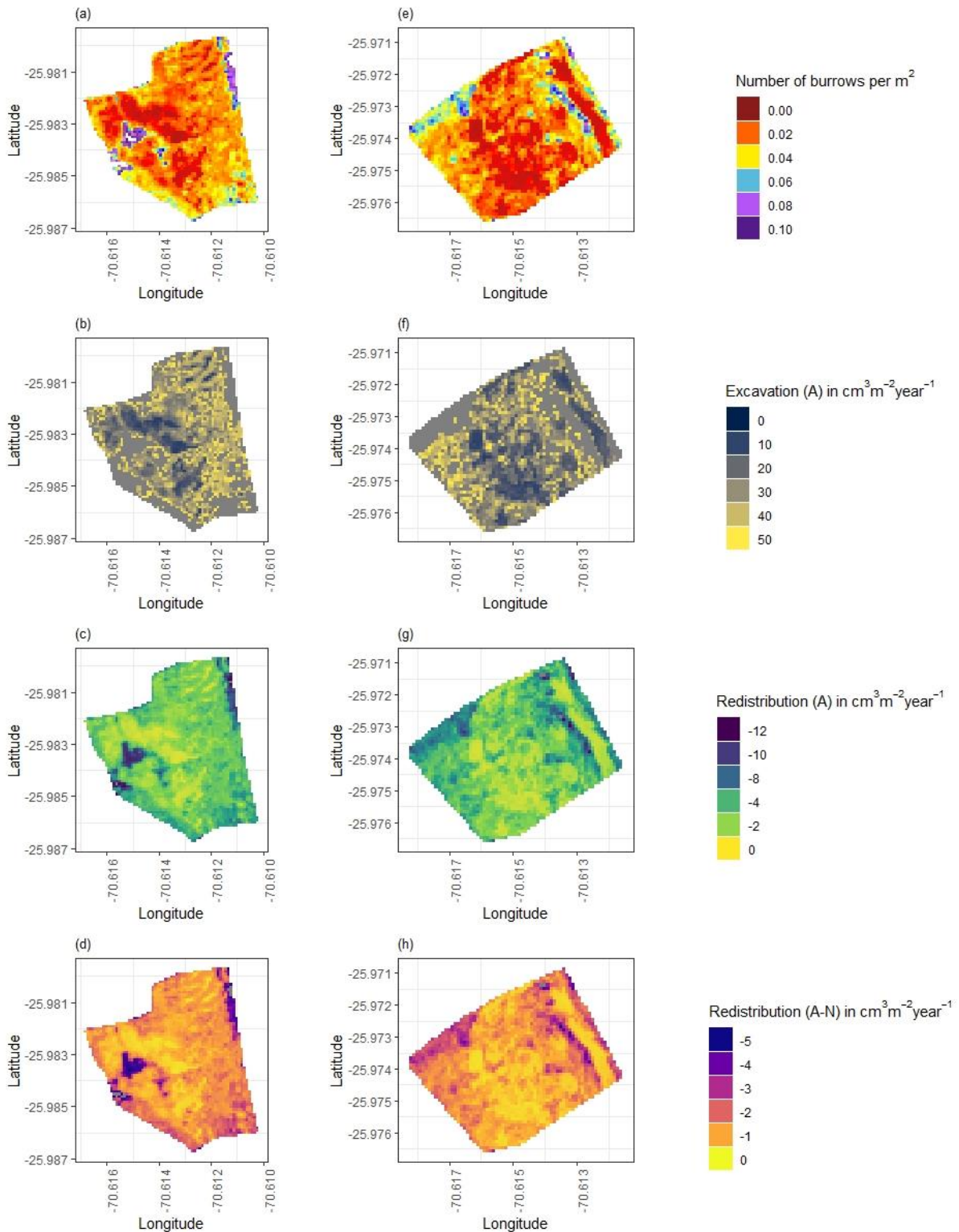
734

Figure A7. Cumulative volume of redistributed sediment for all cameras. Positive values indicate sediment accumulation. Negative values indicate sediment erosion. Whiskers are the median sediment redistribution. E is the burrow entrance. M is the mound. R is burrow roof. UN is area not directly affected by the animal burrowing activity. LC is mediterranean climate zone. PdA is arid climate zone. (a) LC-NU. (b) LC-SU. (c) LC-SL. (d) PdA-NU. (e) PdA-NL. (f) PdA-SU. (g) PdA-SL. For abbreviations see Table A1.



735

736 **Figure A8.** Hillslope-wide volume of redistributed sediment for a time period of one year in LC. (a-d) North-
 737 facing hillslope. (e-h) South-facing hillslope. (a) and (e) Density of burrows as estimated by Grigusova et al.
 738 2021. (b) and (f) Volume of the sediment excavated by the animals. (c) and (g) Volume of the sediment
 739 redistributed during rainfall events within affected areas. (d) and (h) Volume of additionally redistributed
 740 sediment during rainfall events due to presence of the burrows. The values were calculated per burrow as
 741 stated in section 3.7 by subtracting the sediment volume redistributed within animal affected area from the
 742 sediment volume redistributed within not affected area and then upscaled. A stays for affected area, N stays
 743 for not affected area by the burrowing animal.



745

746 **Figure A9.** Hillslope-wide volume of redistributed sediment for a time period of one year in Pan de Azúcar. (a-
 747 d) North-facing hillslope. (e-h) South-facing hillslope. (a) and (e) Density of burrows as estimated by Grigusova
 748 et al. 2021. (b) and (f) Volume of the sediment excavated by the animals. (c) and (g) Volume of the sediment
 749 redistributed during rainfall events within affected areas. (d) and (h) Volume of additionally redistributed
 750 sediment during rainfall events due to presence of the burrows. The values were calculated per burrow as
 751 stated in section 3.7 by subtracting the sediment volume redistributed within animal affected area from the

752 sediment volume redistributed within not affected area and then upscaled. A stays for affected area, N stays
753 for not affected area by the burrowing animal.

754

755 [References](#)

- 756 Afana, A.; Solé-Benet, A.; Pérez, J. L. (2010): Determination of Soil Erosion Using Laser Scanners.
757 Experimental Station of Arid Zone, CSIC, Almeria, Spain, zuletzt geprüft am 22.12.2021.
- 758 Andersen, Douglas C. (1987): Geomys Bursarius Burrowing Patterns: Influence of Season and Food Patch
759 Structure. In: *Ecology* 68 (5), S. 1306–1318. DOI: 10.2307/1939215.
- 760 Ashcroft, Michael B.; Gollan, John R.; Ramp, Daniel (2014): Creating vegetation density profiles for a diverse
761 range of ecological habitats using terrestrial laser scanning. In: *Methods Ecol Evol* 5 (3), S. 263–272. DOI:
762 10.1111/2041-210X.12157.
- 763 BANCROFT, W. J.; HILL, D.; ROBERTS, J. D. (2004): A new method for calculating volume of excavated
764 burrows: the geomorphic impact of Wedge-Tailed Shearwater burrows on Rottneest Island. In: *Funct*
765 *Ecology* 18 (5), S. 752–759. DOI: 10.1111/j.0269-8463.2004.00898.x.
- 766 Bernhard, Nadine; Moskwa, Lisa-Marie; Schmidt, Karsten; Oeser, Ralf A.; Aburto, Felipe; Bader, Maaike Y. et
767 al. (2018): Pedogenic and microbial interrelations to regional climate and local topography: New insights
768 from a climate gradient (arid to humid) along the Coastal Cordillera of Chile. In: *CATENA* 170 (4), S. 335–
769 355. DOI: 10.1016/j.catena.2018.06.018.
- 770 Black, Thomas A.; Montgomery, David R. (1991): Sediment transport by burrowing mammals, Marin County,
771 California. In: *Earth Surf. Process. Landforms* 16 (2), S. 163–172. DOI: 10.1002/esp.3290160207.
- 772 Blanch, Xabier; Eltner, Anette; Guinau, Marta; Abellan, Antonio (2021): Multi-Epoch and Multi-Imagery (MEMI)
773 Photogrammetric Workflow for Enhanced Change Detection Using Time-Lapse Cameras. In: *Remote*
774 *Sensing* 13 (8), S. 1460. DOI: 10.3390/rs13081460.
- 775 Castner, James L.; Fowler, H. G. (1984): Distribution of Mole Crickets (Orthoptera: Gryllotalpidae:
776 Scapteriscus) and the Mole Cricket Parasitoid Larra bicolor (Hymenoptera: Sphecidae) in Puerto Rico. In:
777 *The Florida Entomologist* 67 (3), S. 481. DOI: 10.2307/3494730.
- 778 Cerqueira, Rui (1985): The Distribution of Didelphis in South America (Polyprotodontia, Didelphidae). In:
779 *Journal of Biogeography* 12 (2), S. 135. DOI: 10.2307/2844837.
- 780 Chen, Mingyu; Ma, Li; Shao, Ming'an; Wei, Xiaorong; Jia, Yuhua; Sun, Shuchen et al. (2021): Chinese zokor
781 (Myospalax fontanierii) excavating activities lessen runoff but facilitate soil erosion – A simulation
782 experiment. In: *CATENA* 202 (8), S. 105248. DOI: 10.1016/j.catena.2021.105248.
- 783 Coombes, Martin A. (2016): Biogeomorphology: diverse, integrative and useful. In: *Earth Surf. Process.*
784 *Landforms* 41 (15), S. 2296–2300. DOI: 10.1002/esp.4055.
- 785 Corenblit, Dov; Corbara, Bruno; Steiger, Johannes (2021): Biogeomorphological eco-evolutionary feedback
786 between life and geomorphology: a theoretical framework using fossorial mammals. In: *Die*
787 *Naturwissenschaften* 108 (6), S. 55. DOI: 10.1007/s00114-021-01760-y.
- 788 Eitel, Jan U.H.; Williams, C. Jason; Vierling, Lee A.; Al-Hamdan, Osama Z.; Pierson, Frederick B. (2011):
789 Suitability of terrestrial laser scanning for studying surface roughness effects on concentrated flow erosion
790 processes in rangelands. In: *CATENA* 87 (3), S. 398–407. DOI: 10.1016/j.catena.2011.07.009.
- 791 Eltner, A.; Mulsow, C.; Maas, H.-G. (2013): QUANTITATIVE MEASUREMENT OF SOIL EROSION FROM TLS
792 AND UAV DATA. In: *Int. Arch. Photogramm. Remote Sens. Spatial Inf. Sci.* XL-1/W2, S. 119–124. DOI:

793 10.5194/isprsarchives-XL-1-W2-119-2013.

794 Eltner, A.; Schneider, D.; Maas, H.-G. (2016a): INTEGRATED PROCESSING OF HIGH RESOLUTION
795 TOPOGRAPHIC DATA FOR SOIL EROSION ASSESSMENT CONSIDERING DATA ACQUISITION
796 SCHEMES AND SURFACE PROPERTIES. In: *Int. Arch. Photogramm. Remote Sens. Spatial Inf. Sci.* XLI-
797 B5, S. 813–819. DOI: 10.5194/isprsarchives-XLI-B5-813-2016.

798 Eltner, Anette; Kaiser, Andreas; Abellan, Antonio; Schindewolf, Marcus (2017): Time lapse structure-from-
799 motion photogrammetry for continuous geomorphic monitoring. In: *Earth Surf. Process. Landforms* 42 (14),
800 S. 2240–2253. DOI: 10.1002/esp.4178.

801 Eltner, Anette; Kaiser, Andreas; Castillo, Carlos; Rock, Gilles; Neugirg, Fabian; Abellán, Antonio (2016b):
802 Image-based surface reconstruction in geomorphometry – merits, limits and developments. In: *Earth Surf.*
803 *Dynam.* 4 (2), S. 359–389. DOI: 10.5194/esurf-4-359-2016.

804 Gabet, Emmanuel J.; Reichman, O. J.; Seabloom, Eric W. (2003): The Effects of Bioturbation on Soil
805 Processes and Sediment Transport. In: *Annu. Rev. Earth Planet. Sci.* 31 (1), S. 249–273. DOI:
806 10.1146/annurev.earth.31.100901.141314.

807 Galland, Olivier; Bertelsen, Håvard S.; Guldstrand, Frank; Girod, Luc; Johannessen, Rikke F.; Bjugger, Fanny
808 et al. (2016): Application of open-source photogrammetric software MicMac for monitoring surface
809 deformation in laboratory models. In: *J. Geophys. Res. Solid Earth* 121 (4), S. 2852–2872. DOI:
810 10.1002/2015JB012564.

811 Grigusova, Paulina; Larsen, Annegret; Achilles, Sebastian; Klug, Alexander; Fischer, Robin; Kraus, Diana et
812 al. (2021): Area-Wide Prediction of Vertebrate and Invertebrate Hole Density and Depth across a Climate
813 Gradient in Chile Based on UAV and Machine Learning. In: *Drones* 5 (3), S. 86. DOI:
814 10.3390/drones5030086.

815 Hakonson, T. E. (1999): The Effects of Pocket Gopher Burrowing on Water Balance and Erosion from Landfill
816 Covers. In: *J. environ. qual.* 28 (2), S. 659–665. DOI: 10.2134/jeq1999.00472425002800020033x.

817 Hall, Kevin; Boelhouwers, Jan; Driscoll, Kevin (1999): Animals as Erosion Agents in the Alpine Zone: Some
818 Data and Observations from Canada, Lesotho, and Tibet. In: *Arctic, Antarctic, and Alpine Research* 31 (4),
819 S. 436–446. DOI: 10.1080/15230430.1999.12003328.

820 Hancock, Greg; Lowry, John (2021): Quantifying the influence of rainfall, vegetation and animals on soil erosion
821 and hillslope connectivity in the monsoonal tropics of northern Australia. In: *Earth Surf. Process. Landforms*
822 46 (10), S. 2110–2123. DOI: 10.1002/esp.5147.

823 Hänsel, Phoebe; Schindewolf, Marcus; Eltner, Anette; Kaiser, Andreas; Schmidt, Jürgen (2016): Feasibility of
824 High-Resolution Soil Erosion Measurements by Means of Rainfall Simulations and SfM Photogrammetry.
825 In: *Hydrology* 3 (4), S. 38. DOI: 10.3390/hydrology3040038.

826 Hazelhoff, L.; van Hoof, P.; Imeson, A. C.; Kwaad, F. J. P. M. (1981): The exposure of forest soil to erosion by
827 earthworms. In: *Earth Surf. Process. Landforms* 6 (3-4), S. 235–250. DOI: 10.1002/esp.3290060305.

828 Herbst, M.; Bennett, N. C. (2006): Burrow architecture and burrowing dynamics of the endangered Namaqua
829 dune mole rat (*Bathyergus janetta*) (Rodentia: Bathyergidae). In: *Journal of Zoology* 270 (3), S. 420–428.
830 DOI: 10.1111/j.1469-7998.2006.00151.x.

831 Horn, B.K.P. (1981): Hill shading and the reflectance map. In: *Proc. IEEE* 69 (1), S. 14–47. DOI:
832 10.1109/PROC.1981.11918.

833 Imeson, A. C. (1977): Splash erosion, animal activity and sediment supply in a small forested Luxembourg
834 catchment. In: *Earth Surf. Process. Landforms* 2 (2-3), S. 153–160. DOI: 10.1002/esp.3290020207.

- 835 Imeson, A. C.; Kwaad, F. J. P. M. (1976): Some Effects of Burrowing Animals on Slope Processes in the
836 Luxembourg Ardennes. In: *Geografiska Annaler: Series A, Physical Geography* 58 (4), S. 317–328. DOI:
837 10.1080/04353676.1976.11879941.
- 838 Iserloh, T.; Ries, J. B.; Arnáez, J.; Boix-Fayos, C.; Butzen, V.; Cerdà, A. et al. (2013): European small portable
839 rainfall simulators: A comparison of rainfall characteristics. In: *CATENA* 110 (2), S. 100–112. DOI:
840 10.1016/j.catena.2013.05.013.
- 841 James, M. R.; Robson, S. (2014): Sequential digital elevation models of active lava flows from ground-based
842 stereo time-lapse imagery. In: *ISPRS Journal of Photogrammetry and Remote Sensing* 97 (3), S. 160–
843 170. DOI: 10.1016/j.isprsjprs.2014.08.011.
- 844 Jimenez, J. E.; Feinsinger, P.; Jaksi, F. M. (1992): Spatiotemporal Patterns of an Irruption and Decline of Small
845 Mammals in Northcentral Chile. In: *Journal of Mammalogy* 73 (2), S. 356–364. DOI: 10.2307/1382070.
- 846 Jones, Clive G.; Gutiérrez, Jorge L.; Byers, James E.; Crooks, Jeffrey A.; Lambrinos, John G.; Talley, Theresa
847 S. (2010): A framework for understanding physical ecosystem engineering by organisms. In: *Oikos* 119
848 (12), S. 1862–1869. DOI: 10.1111/j.1600-0706.2010.18782.x.
- 849 Kaiser, Andreas; Neugirg, Fabian; Rock, Gilles; Müller, Christoph; Haas, Florian; Ries, Johannes; Schmidt,
850 Jürgen (2014): Small-Scale Surface Reconstruction and Volume Calculation of Soil Erosion in Complex
851 Moroccan Gully Morphology Using Structure from Motion. In: *Remote Sensing* 6 (8), S. 7050–7080. DOI:
852 10.3390/rs6087050.
- 853 Kinlaw, A.; Grasmueck, M. (2012): Evidence for and geomorphologic consequences of a reptilian ecosystem
854 engineer: The burrowing cascade initiated by the Gopher Tortoise. In: *Geomorphology* 157-158 (4), S.
855 108–121. DOI: 10.1016/j.geomorph.2011.06.030.
- 856 Kromer, Ryan; Walton, Gabe; Gray, Brian; Lato, Matt; Group, Robert (2019): Development and Optimization
857 of an Automated Fixed-Location Time Lapse Photogrammetric Rock Slope Monitoring System. In: *Remote*
858 *Sensing* 11 (16), S. 1890. DOI: 10.3390/rs11161890.
- 859 Kukko, Antero; Hyypä, Juha (2009): Small-footprint Laser Scanning Simulator for System Validation, Error
860 Assessment, and Algorithm Development. In: *photogramm eng remote sensing* 75 (10), S. 1177–1189.
861 DOI: 10.14358/PERS.75.10.1177.
- 862 Larsen, A.; Nardin, W.; Lageweg, W. I.; Bätz, N. (2021): Biogeomorphology, quo vadis? On processes, time,
863 and space in biogeomorphology. In: *Earth Surf. Process. Landforms* 46 (1), S. 12–23. DOI:
864 10.1002/esp.5016.
- 865 Le Hir, P.; Monbet, Y.; Orvain, F. (2007): Sediment erodability in sediment transport modelling: Can we account
866 for biota effects? In: *Continental Shelf Research* 27 (8), S. 1116–1142. DOI: 10.1016/j.csr.2005.11.016.
- 867 Lehnert, Lukas W.; Thies, Boris; Trachte, Katja; Achilles, Sebastian; Osses, Pablo; Baumann, Karen et al.
868 (2018): A Case Study on Fog/Low Stratus Occurrence at Las Lomitas, Atacama Desert (Chile) as a Water
869 Source for Biological Soil Crusts. In: *Aerosol Air Qual. Res.* 18 (1), S. 254–269. DOI:
870 10.4209/aaqr.2017.01.0021.
- 871 Li, Guorong; Li, Xilai; Li, Jinfang; Chen, Wenting; Zhu, Haili; Zhao, Jianyun; Hu, Xiasong (2019a): Influences
872 of Plateau Zokor Burrowing on Soil Erosion and Nutrient Loss in Alpine Meadows in the Yellow River
873 Source Zone of West China. In: *Water* 11 (11), S. 2258. DOI: 10.3390/w11112258.
- 874 Li, Larry (2014): Time-of-Flight Camera – An Introduction. Technical White Paper. Hg. v. Texas Instruments.
875 Online verfügbar unter <https://www.ti.com/lit/wp/sloa190b/sloa190b.pdf>, zuletzt geprüft am 22.12.2021.
- 876 Li, T. C.; Shao, M. A.; Jia, Y. H.; Jia, X. X.; Huang, L. M.; Gan, M. (2019b): Small-scale observation on the

877 effects of burrowing activities of ants on soil hydraulic processes. In: *Eur J Soil Sci* 70 (2), S. 236–244.
878 DOI: 10.1111/ejss.12748.

879 Li, Tongchuan; Jia, Yuhua; Shao, Ming'an; Shen, Nan (2019c): *Camponotus japonicus* burrowing activities
880 exacerbate soil erosion on bare slopes. In: *Geoderma* 348 (4), S. 158–167. DOI:
881 10.1016/j.geoderma.2019.04.035.

882 Li, Tongchuan; Shao, Ming'an; Jia, Yuhua; Jia, Xiaoxu; Huang, Laiming (2018): Small-scale observation on the
883 effects of the burrowing activities of mole crickets on soil erosion and hydrologic processes. In: *Agriculture,*
884 *Ecosystems & Environment* 261 (4), S. 136–143. DOI: 10.1016/j.agee.2018.04.010.

885 Longoni, Laura; Papini, Monica; Brambilla, Davide; Barazzetti, Luigi; Roncoroni, Fabio; Scaioni, Marco; Ivanov,
886 Vladislav (2016): Monitoring Riverbank Erosion in Mountain Catchments Using Terrestrial Laser Scanning.
887 In: *Remote Sensing* 8 (3), S. 241. DOI: 10.3390/rs8030241.

888 MALLALIEU, JOSEPH; CARRIVICK, JONATHAN L.; QUINCEY, DUNCAN J.; SMITH, MARK W.; JAMES,
889 WILLIAM H.M. (2017): An integrated Structure-from-Motion and time-lapse technique for quantifying ice-
890 margin dynamics. In: *J. Glaciol.* 63 (242), S. 937–949. DOI: 10.1017/jog.2017.48.

891 Meysman, Filip J. R.; Boudreau, Bernard P.; Middelburg, Jack J. (2003): Relations between local, nonlocal,
892 discrete and continuous models of bioturbation. In: *Journal of Marine Research* 61 (3), S. 391–410. DOI:
893 10.1357/002224003322201241.

894 Morris, Rowena H.; Buckman, Solomon; Connelly, Paul; Dragovich, Deirdre; Ostendorf, Bertram; and
895 Bradstock, Ross A. (2011): The dirt on assessing post-fire erosion in the Mount Lofty Ranges: comparing
896 methods.

897 Muñoz-Pedrerros, Andrés; Yáñez, José; Norambuena, Heraldo V.; Zúñiga, Alfredo (2018): Diet, dietary
898 selectivity and density of South American grey fox, *Lycalopex griseus*, in Central Chile. In: *Integrative*
899 *zoology* 13 (1), S. 46–57. DOI: 10.1111/1749-4877.12260.

900 Nasermoaddeli, M. B.; Pasche, E. (2008): Application of terrestrial 3D scanner in quantification of the riverbank
901 erosion and deposition. Institute of river and coastal engineering, Technical university Hamburg-Harburg,
902 Hamburg,. Online verfügbar unter [https://www.tuhh.de/t3resources/wb/Publikationen/MA-](https://www.tuhh.de/t3resources/wb/Publikationen/MA-Veroeffentlichungen/nasermoaddeli/riverflow2008.pdf)
903 [Veroeffentlichungen/nasermoaddeli/riverflow2008.pdf](https://www.tuhh.de/t3resources/wb/Publikationen/MA-Veroeffentlichungen/nasermoaddeli/riverflow2008.pdf), zuletzt geprüft am 22.12.2021.

904 Pang, Xiao Pan; Guo, Zheng Gang (2017): Plateau pika disturbances alter plant productivity and soil nutrients
905 in alpine meadows of the Qinghai-Tibetan Plateau, China. In: *Rangel. J.* 39 (2), S. 133. DOI:
906 10.1071/RJ16093.

907 Reichman, O. J.; Seabloom, Eric W. (2002): The role of pocket gophers as subterranean ecosystem engineers.
908 In: *Trends in Ecology & Evolution* 17 (1), S. 44–49. DOI: 10.1016/S0169-5347(01)02329-1.

909 Richards, Paul J.; Humphreys, Geoff S. (2010): Burial and turbulent transport by bioturbation: a 27-year
910 experiment in southeast Australia. In: *Earth Surf. Process. Landforms* 21 (2), n/a-n/a. DOI:
911 10.1002/esp.2007.

912 Ridd, Peter V. (1996): Flow Through Animal Burrows in Mangrove Creeks. In: *Estuarine, Coastal and Shelf*
913 *Science* 43 (5), S. 617–625. DOI: 10.1006/ecss.1996.0091.

914 Romañach, Stephanie S.; Reichman, O. J.; Seabloom, E. W. (2005): Seasonal influences on burrowing activity
915 of a subterranean rodent, *Thomomys bottae*. In: *Journal of Zoology* 266 (3), S. 319–325. DOI:
916 10.1017/S0952836905006941.

917 Rutin, J. (1996): The burrowing activity of scorpions (*Scorpio maurus palmatus*) and their potential contribution
918 to the erosion of Hamra soils in Karkur, central Israel. In: *Geomorphology* 15 (2), S. 159–168. DOI:

919 10.1016/0169-555X(95)00120-T.

920 Sarbolandi, Hamed; Plack, Markus; Kolb, Andreas (2018): Pulse Based Time-of-Flight Range Sensing. In:
921 *Sensors (Basel, Switzerland)* 18 (6). DOI: 10.3390/s18061679.

922 Schiffers, Katja; Teal, Lorna Rachel; Travis, Justin Mark John; Solan, Martin (2011): An open source simulation
923 model for soil and sediment bioturbation. In: *PloS one* 6 (12), e28028. DOI: 10.1371/journal.pone.0028028.

924 Sharon, David (1980): The distribution of hydrologically effective rainfall incident on sloping ground. In: *Journal*
925 *of Hydrology* 46 (1-2), S. 165–188. DOI: 10.1016/0022-1694(80)90041-4.

926 Thomsen, L. M.; Baartman, J. E. M.; Barneveld, R. J.; Starkloff, T.; Stolte, J. (2015): Soil surface roughness:
927 comparing old and new measuring methods and application in a soil erosion model. In: *SOIL* 1 (1), S. 399–
928 410. DOI: 10.5194/soil-1-399-2015.

929 Übernichel, Kirstin; Ehlers, Todd A.; Paulino, Leandro; Fuentes Espoz, Juan-Pablo (2021a): Time series of
930 meteorological stations on an elevational gradient in National Park La Campana, Chile. Unter Mitarbeit von
931 Kirstin Übernichel, Todd A. Ehlers, Leandro Paulino, Juan-Pablo Fuentes Espoz, Ramiro Bernales-
932 Noguera, Willi Kappler et al.

933 Übernichel, Kirstin; Pizarro-Araya, Jaime; Bhagavathula, Susila; Paulino, Leandro; Ehlers, Todd A. (2021b):
934 Reviews and syntheses: Composition and characteristics of burrowing animals along a climate and
935 ecological gradient, Chile. In: *Biogeosciences* 18 (20), S. 5573–5594. DOI: 10.5194/bg-18-5573-2021.

936 Voiculescu, Mircea; Ianăș, Ana-Neli; Germain, Daniel (2019): Exploring the impact of snow vole (*Chionomys*
937 *nivalis*) burrowing activity in the Făgăraș Mountains, Southern Carpathians (Romania): Geomorphic
938 characteristics and sediment budget. In: *CATENA* 181 (1), S. 104070. DOI: 10.1016/j.catena.2019.05.016.

939 Wei, Xinghu; Li, Sen; Yang, Ping; Cheng, Huaishun (2007): Soil erosion and vegetation succession in alpine
940 Kobresia steppe meadow caused by plateau pika—A case study of Nagqu County, Tibet. In: *Chin.*
941 *Geograph.Sc.* 17 (1), S. 75–81. DOI: 10.1007/s11769-007-0075-0.

942 Wilkinson, Marshall T.; Richards, Paul J.; Humphreys, Geoff S. (2009): Breaking ground: Pedological,
943 geological, and ecological implications of soil bioturbation. In: *Earth-Science Reviews* 97 (1-4), S. 257–
944 272. DOI: 10.1016/j.earscirev.2009.09.005.

945 Yair, A. (1995): Short and long term effects of bioturbation on soil erosion, water resources and soil
946 development in an arid environment. In: *Geomorphology* 13 (1-4), S. 87–99. DOI: 10.1016/0169-
947 555X(95)00025-Z.

948 Yoo, Kyungsoo; Amundson, Ronald; Heimsath, Arjun M.; Dietrich, William E. (2005): Process-based model
949 linking pocket gopher (*Thomomys bottae*) activity to sediment transport and soil thickness. In: *Earth Surf.*
950 *Process. Landforms* 33 (11), S. 917. DOI: 10.1130/G21831.1.

951